TÜBİTAK

Turkish Journal of Earth Sciences

http://journals.tubitak.gov.tr/earth/

Research Article

Turkish J Earth Sci
(2020) 29: 1073-1099

doi:10.3906/yer-1912-15

Epidote – lawsonite coexistence in blueschist-facies block from the Tavşanlı Zone – Turkey: petrological implications

Mete ÇETİNKAPLAN*

Department of Geological Engineering, Faculty of Engineering, Dokuz Eylül University, İzmir, Turkey

Received: 29.12.2019 • **Accepted/Published Online:** 18.08.2020 • **Final Version:** 16.11.2020

Abstract: Metamorphic evolution of an epidote–lawsonite blueschist sample characterized by the coexistence of lawsonite and epidote from Sivrihisar area (Tavşanlı Zone) was studied herein in terms of petrology and mineral equilibria. Based on the textural evidence and phase composition, 2 prograde stages, defined by assemblage-I and -II, and 1 retrograde stage were recognized. Assemblage-I indicates epidote-blueschist facies conditions (12 ± 1 kbar / 485 ± 10 °C). Assemblage-II is characterized by the coexistence of epidote and lawsonite (17 ± 1 kbar / 515 ± 10 °C) corresponding to the interface of lawsonite blueschist and epidote blueschist facies. Phase diagram calculations and mineral compositions revealed that along this interface, an equilibrium field with lawsonite and epidote is stable. This closed-equilibrium field is controlled by high aH_2O and an elevated Fe^{3+}/Al ratio of minerals. Pressure-temperature (P–T) estimates and textural observations indicated a counter-clockwise path during the subduction and exhumation history. The preservation of lawsonite and epidote during the retrograde stage pointed to the fact that the path followed the stability field of lawsonite and epidote during exhumation.

Key words: Lawsonite-epidote equilibrium, metamorphic evolution, Tavşanlı Zone, blueschist, XMapTools

1. Introduction

Eclogite–blueschist belts mark ancient convergent margins. Because lawsonite can provide an understanding of the dynamics of a subduction-zone channel overlying the descending slab, the existence of lawsonite in such tectonic settings is of special interest (Wei and Clarke, 2011; Tsujimori and Ernst, 2014; Vitale Brovarone et al., 2014; Agard et al., 2018). Lawsonite is only stable under high pressure/low temperature (HP/LT) conditions and thus, is restricted to subduction zones (Zack et al., 2004; Martin et al., 2014; Fornash et al., 2018). Most fragments of subducted crust that reach the Earth's surface are heated during exhumation and thus, lose their former low-temperature/high-pressure assemblage (Schmidt and Poli, 1994). Consequently, in many blueschist/eclogite locations, lawsonite was retrogressed to epidote during decompression and exhumation as the result of thermal relaxation (e.g., Bearth, 1973; Ernst and Dal Piaz, 1978; Pognante, 1989; Ballevre et al., 2003). In order to avoid the thermal relaxation effects, the exhumation process must be faster than usual (Ernst, 1988) and the retrograde path should not leave the stability field of lawsonite (Zack et al., 2004). Lawsonite blueschist and epidote blueschist facies are characterized by lawsonite + glaucophane and epidote + glaucophane paragenesis, respectively (Evans, 1990). In general, the univariant line separating lawsonite from epidote in the blueschist facies is defined by a positive Clapeyron slope (Tsujimori and Ernst, 2014). However, because of the compositional difference between these 2 phases, and minor changes in fO_2 during blueschist facies metamorphism, lawsonite and epidote coexistence can be observed within a narrow stability field along the epidote and lawsonite blueschist facies interface (Brown, 1977; Enami et al., 2004; Poli and Schmidt, 2004). In addition to fO_2 and X_{CO2}, differences in the bulk composition may control the occurrence of lawsonite or epidote in different parts of a single outcrop (Enami et al., 2004). Highly oxidizing conditions are expected to maximize epidote stability (Poli and Schmidt, 2004). If magnetite or hematite is included in blueschist-facies boundary reactions, the P–T field of blueschist facies expands (Banno and Sakai, 1989). Chlorite and calcite at high X_{CO2} cause the destabilization of the coexisting epidote–lawsonite (Enami et al., 2004).

In Turkey, blueschist localities, except for those associated with the retrogression of eclogite during exhumation, are quite common. These locations can be divided into 3 main groups according to their distinctive key

* Correspondence: mete.cetinkaplan@deu.edu.tr

mineral content: 1) carpholite-, 2) epidote-, 3) lawsonite-/epidote-bearing. The Afyon Zone/Lycian nappes (Oberhänsli et al., 2001; Candan et al., 2005; Rimmele et al., 2005), Menderes Massif (cover series) (Candan et al., 2005; Rimmele et al., 2005), and Bitlis Massif (cover sequence) (Oberhänsli et al., 2010) are carpholite-bearing. The Alanya Massif (Gündoğmuş) (Okay, 1986; Çetinkaplan et al., 2016) and Cycladic Blueschist Unit (Dilek Peninsula-Selçuk) (Oberhänsli et al., 1998; Candan et al., 1997; Çetinkaplan et al., 2020) have been metamorphosed under epidote-blueschist facies conditions. The Biga Peninsula (Topuz et al., 2008) and Tavşanlı Zone (Okay, 1980, 1986, 2002; Davis and Whitney, 2006, 2008) are rare places where lawsonite blueschist and epidote blueschist facies can be observed. The east–west trending metamorphic belt in the northernmost Anatolides is called the Tavşanlı Zone. It occurs immediately south of the İzmir-Ankara-Erzincan suture zone in Turkey (Figures 1a and 1b; Okay, 1984a, 1984b, 2002). In the Sivrihisar area (Tavşanlı Zone), lawsonite-bearing eclogites and blueschists occur as tectonic blocks in a blueschist to an eclogite bearing accretionary complex (Davis and Whitney, 2006, 2008; Whitney and Davis, 2006; Çetinkaplan et al., 2008; Davis, 2011). These rocks show tabular lawsonite as euhedral individual crystal in either aglaucophane or omphacite-rich matrix. Davis and Whitney (2006, 2008) and Whitney and Davis (2006) pointed to the coexistence of lawsonite–epidote in some of these rocks.

In general, the epidote–lawsonite transition is defined by a univariant line. Whereas, in the Sivrihisar area, the textural evidence indicates an equilibrium between epidote and lawsonite. The aim of this study was to investigate the factors that stabilize the epidote–lawsonite equilibrium, which can be defined as a transition in a closed equilibrium field.

2. Geological setting

2.1. Geology of Tavşanlı Zone

The main metamorphic units of the Anatolides in western Anatolia are from north to south: the Tavşanlı Zone, the Afyon Zone, the Menderes Massif, and the Lycian nappes. The Tavşanlı Zone, described as a typical blueschist zone (Okay, 1980,1982, 1984a, 1984b, 1986; Okay et al., 1998; Okay, 2002, Figure 1b), was derived from the northernmost part of the Anatolide–Tauride platform and is crucial for understanding the subduction and exhumation processes of the Neotethys. The Tavşanlı Zone can be separated into 4 tectonic units (Okay, 1984a, 1984b; Okay, 2002; Çetinkaplan et al., 2008): 1) coherent blueschist sequence, 2) blueschist to eclogite accretionary complex, 3) Cretaceous accretionary complex with incipient blueschist metamorphism, and 4) non-metamorphic ophiolitic slab (Figure 1b). The coherent blueschist sequence, presenting exhumed passive continental margin sediments (Okay, 2002), consists of metamorphic clastic rocks at the base and conformable overlying marbles (Okay, 1984a, 1984b; Çetinkaplan et al., 2008). Metamorphic clastic rocks, probably Triassic in age, are composed of graphitic schists and phyllites with jadeite, glaucophane, lawsonite, and chloritoid assemblages (Okay and Kelley, 1994). They record one of the lowest geothermal gradients (5 °C km^{-1}) in the world (Okay and Kelley,1994; Okay, 2002). Marbles of several kilometers in thicknesses contain fibrous rod-shaped calcite (aragonite pseudomorph) (Seaton et al., 2009; Sheffler et al., 2015) crystals and pass to cherty marbles at the uppermost levels (Okay, 1986). The coherent sequence is tectonically overlain by a blueschist to eclogite facies accretionary complex (Çetinkaplan et al., 2008). The dominant lithologies are made up of epidote-glaucophane blueschist metabasite, metachert, serpentinite and more rarely, neritic metacarbonate. In only 1 locality (Sivrihisar) has the existence of lawsonite and epidote eclogites been reported (Davis and Whitney, 2006, 2008; Whitney and Davis, 2006; Çetinkaplan et al., 2008; Davis, 2011). The Cretaceous accretionary complex is composed of pelagic shale, basalt, radiolarian chert, tectonized serpentinite, and reddish pelagic limestone with aragonite (Topuz and Okay, 2014). Recently, the existence of carpholite has been documented in this accretionary complex (Plunder et al., 2013). Large tectonic slabs of ophiolite, predominantly peridotite with rare gabbroic veins, lie over the blueschist and Cretaceous accretionary complexes (Okay, 1984a). These ophiolites have not experienced the Alpine high-pressure/low-temperature metamorphism and represent the obducted oceanic lithosphere of the Neo-Tethyan Ocean (Okay,1984a, 1984b).

Jadeite–chloritoid–glaucophane–lawsonite paragenesis in metapelites indicate metamorphic conditions of 24 ± 3 kbar and 430 ± 30 °C for the Cretaceous blueschist metamorphism in the coherent sequence of the Tavşanlı Zone (Okay, 2002). The blueschist to eclogite accretionary complex in Sivrihisar is 1 of only 19 known lawsonite eclogite localities in the word (Tsujimori and Ernst, 2014). In this area, different P–T conditions were obtained from mafic rock types, despite similar bulk composition (Davis and Whitney, 2006). The P–T conditions recorded from mafic rocks in the accretionary complex were 22–24 kbar, 520 °C for lawsonite eclogite (Davis and Whitney, 2008), 24 ± 1 kbar, 460 ± 25 °C for lawsonite eclogite (Çetinkaplan et al., 2008), 18 kbar, 600 °C for epidote eclogite (Davis and Whitney, 2006), 12 kbar, 380 °C for lawsonite blueschist (Davis and Whitney, 2006), and 15–16 kbar, 480–500 °C for lawsonite-epidote blueschist (Davis and Whitney, 2006). The P–T conditions and anticlockwise paths of the rocks show a distribution according to the stability fields of lawsonite or epidote and/or the coexistence of

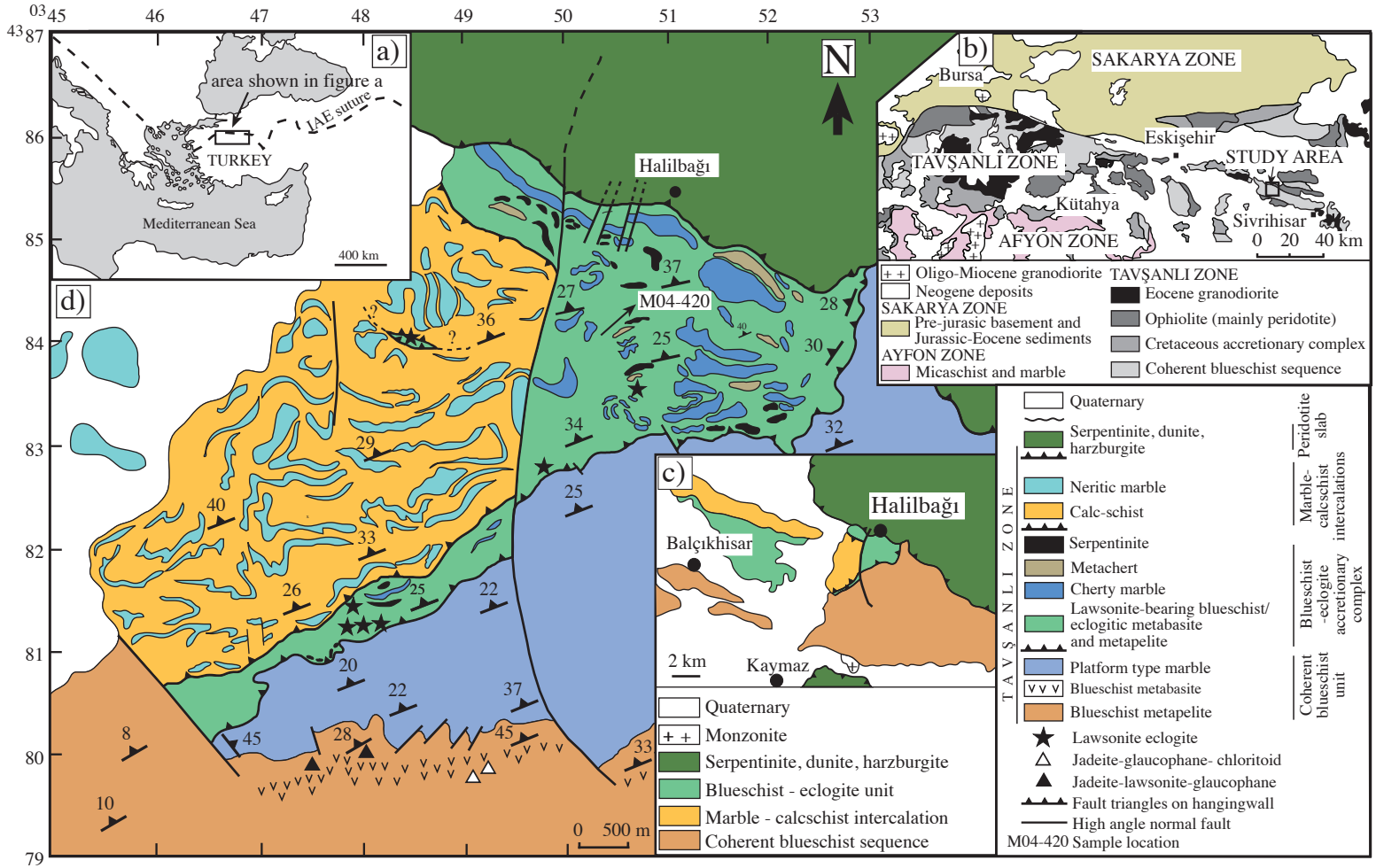

Figure 1. a) Location of the Tavşanlı Zone in western Anatolia; b) regional distribution of blueschists in the Tavşanlı Zone, between the Sakarya Zone and the Afyon Zone (Okay, 2002); c) simplified geologic map showing the main units in the region around the studied area; and d) geologic map of the Sivrihisar area. IAE: İzmir-Ankara-Erzincan suture.

epidote–lawsonite assemblages (Davis and Whitney, 2006; Davis and Whitney, 2008). These exhumation loops of the high-pressure rocks are close to the epidote–lawsonite boundary (e.g., Figure 17; Davis and Whitney, 2006). The preservation of lawsonite indicates that the retrograde P–T path remained in the stability field of lawsonite during exhumation (Çetinkaplan et al., 2008). The regional preservation of lawsonite in blueschist and eclogites records an extremely low geothermal gradient (5–6 °C km^{-1}) and rapid exhumation (Okay, 2002; Davis and Whitney, 2006; Whitney and Davis, 2006; Çetinkaplan et al., 2008).

2.2. Lithostratigraphy of the study area

The generalized rock succession of the Sivrihisar study area consists, from bottom to top, of 1) a coherent blueschist unit (metaclastics and overlying marbles), 2) a blueschist-eclogite accretionary complex, 3) marble–calcschists intercalations, and 4) a non-metamorphic peridotite slab (Figures 1c and 1d). Metaclastic rocks are characterized by the assemblage phengite, jadeite, lawsonite, and glaucophane (Okay, 2002; Çetinkaplan et al., 2008). At the top, they contain metabasic-rich levels, which show lateral continuation over several kilometers. They consist of jadeite, chloritoid, and glaucophane. Rod-shaped calcite-bearing platform-type marbles, up to 1500-m-thick, overlay the metaclastic sequence with gradational contact, marked by the appearance of thin marble layers within the mica schists. The marbles are tectonically overlain by a blueschist-eclogite accretionary complex. It is composed of predominantly metabasic rocks (>70%) consisting of lawsonite or epidote eclogite, eclogitic metabasite (less than 70% garnet + omphacite), lawsonite blueschist, omphacite-lawsonite blueschist, and metagabbro blocks. The major element composition of these mafic rocks has similar bulk composition, equivalent to normal mid-ocean ridge basalts (Davis and Whitney, 2006). However, the maximum pressure-temperature conditions of these rocks differ from each other in relation to the burial depth and they represent a wide P–T range (26–12 kbar/520–380°C; Davis and Whitney, 2006; Pourteau et al., 2019). The mafic rocks recording different maximum P–T conditions were tectonically juxtaposed as high-P pods (Davis and Whitney, 2006). The age of the high-pressure metamorphism of the lawsonite eclogite is 90 ± 1.4 to 93 ± 1.8 Ma, dated by Ar-Ar on phengite (Fornash et al., 2016). The Lu-Hf garnet data from the epidote eclogite and lawsonite-epidote blueschist yielded an identical Late Cretaceous age (92 ± 0.2 Ma, Pourteau et al., 2019/91 ± 1.3 Ma; Mulcahy et al., 2014) and 90 ± 0.5 Ma (Pourteau et al., 2019), respectively. The retrograde overprint was dated at 86 ± 0.3 Ma (Lu-Hf garnet) for a lawsonite blueschist (Pourteau et al., 2019). Blocks of thin pelagic marble, cherty marble, meta-chert, neritic marble, metamorphic serpentinite, and blueschist metapelite constitute the other lithologies of the accretionary complex. Marble–calcschist intercalations of more than 200-m-thick form the uppermost tectonic unit of the metamorphic succession. These intercalations are characterized by strongly deformed and boudinaged marble and calcschist layers rich in white mica, chlorite, calcite, and quartz. A peridotite slab forms the uppermost tectonic unit (Figure 1d). It consists of massive and homogeneous dunite, harzburgite, and serpentinite. Detailed petrographical descriptions of these lithological/tectonic units were given by Davis and Whitney (2006), Davis and Whitney (2008), and Çetinkaplan et al., (2008).

2.3. Field observations of the sample

The investigated epidote–lawsonite blueschist sample (M04-420) was taken from a lens-shaped blueschist-facies block, 3 × 2 m in size, occurring in the blueschist-eclogite accretionary complex (Figure 1d). The long axes of the lens-shaped block parallel the foliation of the accretionary complex (NE–SW). This massive block is located in strongly foliated and altered blueschists. Although the block displays chlorite-rich zones at the contact point to the host rock, its inner parts are massive. There is no obvious folding. The block contains garnet, omphacite, glaucophane, lawsonite, epidote, phengite, and rutile. Chlorite is a secondary mineral. The regional foliation of the block is dominantly defined by a parallel alignment of the prismatic glaucophane and omphacite crystals. Garnet and lawsonite grains, up to 2 mm in size, responsible for a marked surface roughness, can easily be recognized in the field. White rectangular lawsonite and green epidote crystals, up to 1 mm, show a homogeneous distribution in a glaucophane-rich matrix. In this matrix, the modal volume of garnet and omphacite is macroscopically less than 70%. In the field, this rare mafic rock type (Davis and Whitney, 2006; Davis and Whitney, 2008; Pourteau et al., 2019) is distinguished from the other rocks by the coexistence of epidote and lawsonite.

3. Petrography and mineral chemistry

Electron microprobe studies were performed with a JEOL 8900 microprobe (Akishima, Tokyo, Japan) at Potsdam University. Operating conditions were 15 kV acceleration voltage, a 15 nA beam current, and a counting time of 20–30 s. The beam diameter was set to 2–5 μm. Natural minerals were used for standardization. The raw data were corrected using the ZAF method. Fe^{3+} values of the minerals were determined using stoichiometry. Optically negative, monoclinic, and iron-rich [Pistacite (Ps): >20 mol%); (Ps =100*Fe^{3+} /(Fe^{3+} + Al)] epidote group minerals were reported as epidote. Representative mineral analyses are given in Tables 1–7. When the standard deviation in the analysis was evaluated considering the different generations of each mineral, the standard deviation remained limited between 0.07 and 0.02. The mineral

Table 1. Representative garnet analyses.

	Grt-II			r.z.	Grt-I						
SiO_2	37.33	37.25	37.30	37.15	37.58	37.57	37.76	37.24	37.65	37.79	37.39
TiO_2	0.05	0.10	0.07	0.04	0.11	0.09	0.14	0.19	0.06	0.10	0.06
Al_2O_3	21.26	21.19	21.13	21.23	21.46	21.50	21.22	21.49	21.43	21.45	21.78
FeO_{tot}	29.43	29.10	28.24	24.52	28.11	28.13	27.90	27.86	27.48	28.18	28.64
MnO	0.79	1.09	2.17	6.86	1.41	1.90	2.04	2.39	2.45	1.88	1.60
MgO	2.02	1.75	1.58	1.20	2.85	2.54	2.34	2.40	2.35	2.70	2.90
CaO	8.59	8.93	8.71	8.04	7.85	8.00	8.29	7.94	8.31	7.70	7.37
Na_2O	0.03	0.02	0.02	0.02	0.04	0.04	0.02	0.04	0.03	0.02	0.02
K_2O	0.00	0.01	0.01	0.01	0.00	0.01	0.00	0.01	0.00	0.00	0.01
Sum	99.49	99.42	99.22	99.07	99.41	99.77	99.70	99.55	99.76	99.81	99.78
24 oxygens											
Si	5.98	5.98	6.00	6.00	5.99	5.98	6.01	5.95	5.99	6.00	5.95
Ti	0.01	0.01	0.01	0.00	0.01	0.01	0.02	0.02	0.01	0.01	0.01
Al	4.01	4.01	4.01	4.04	4.03	4.03	3.98	4.05	4.02	4.02	4.08
Fe^{2+}	3.94	3.89	3.79	3.30	3.74	3.74	3.72	3.72	3.66	3.74	3.81
Fe^{3+}	0.00	0.01	0.01	0.01	0.00	0.00	0.00	0.00	0.00	0.00	0.00
Mn	0.11	0.15	0.30	0.94	0.19	0.26	0.28	0.32	0.33	0.25	0.22
Mg	0.48	0.42	0.38	0.29	0.68	0.60	0.56	0.57	0.56	0.64	0.69
Ca	1.47	1.54	1.50	1.39	1.34	1.36	1.41	1.36	1.42	1.31	1.26
Na	0.01	0.01	0.01	0.01	0.01	0.01	0.01	0.01	0.01	0.00	0.01
K	0.00	0.00	0.00	0.00	0.00	0.00	0.00	0.00	0.00	0.00	0.00
Sum	16.01	16.01	15.99	15.98	15.99	16.00	15.98	16.01	15.99	15.98	16.01
Alm(%)	66	65	64	56	63	63	62	62	61	63	64
Prp(%)	8	7	6	5	11	10	9	10	9	11	12
Sps(%)	2	2	5	16	3	4	5	5	6	4	4
Grs(%)	25	26	25	23	23	23	24	23	24	22	21
X_{Mg}	0.11	0.10	0.09	0.08	0.15	0.14	0.13	0.13	0.13	0.15	0.15
	Grt-I	r.z.	Grt-II								
SiO_2	37.53	37.33	37.10	37.23	37.36						
TiO_2	0.03	0.05	0.08	0.06	0.08						
Al_2O_3	21.63	21.22	21.32	21.13	21.24						
FeO_{tot}	28.62	25.74	24.67	29.18	29.67						
MnO	1.18	5.81	7.13	1.08	1.07						
MgO	3.24	1.53	1.20	1.78	1.82						
CaO	7.38	8.19	7.54	8.80	8.50						
Na_2O	0.01	0.01	0.04	0.02	0.00						
K_2O	0.00	0.00	0.00	0.00	0.01						
Sum	99.63	99.09	99.09	99.27	99.74						
24 oxygens											
Si	5.96	5.98	5.99	5.98	5.98						
Ti	0.00	0.01	0.01	0.01	0.01						
Al	4.05	4.01	4.06	4.00	4.01						
Fe^{2+}	3.80	3.44	3.32	3.91	3.97						

Table 1. (Continued).

Fe^{3+}	0.00	0.01	0.01	0.01	0.00						
Mn	0.16	0.79	0.97	0.15	0.14						
Mg	0.77	0.36	0.29	0.43	0.43						
Ca	1.26	1.41	1.30	1.51	1.46						
Na	0.00	0.00	0.01	0.01	0.00						
K	0.00	0.00	0.00	0.00	0.00						
Sum	16.01	16.01	15.98	16.01	16.01						
Alm(%)	64	57	56	65	66						
Prp(%)	13	6	5	7	7						
Sps(%)	3	13	17	2	2						
Grs(%)	21	23	22	25	24						
X_{Mg}	0.17	0.10	0.08	0.10	0.10						

Alm: $Fe^{2+}/(Fe^{2+}+Mg+Ca+Mn)$, Prp: $Mg/(Fe^{2+}+Mg+Ca+Mn)$, Grs: $Ca/(Fe^{2+}+Mg+Ca+Mn)$,
Sps: $Mn/(Fe^{2+}+Mg+Ca+Mn)$.
r.z.: Resorption zone.

Table 2. Representative chlorite analyses.

	Chl-I						Chl-II		
SiO_2	26.75	26.49	26.92	26.46	27.01	26.64	27.55	27.22	27.65
TiO_2	0.00	0.01	0.00	0.00	0.00	0.02	0.00	0.02	0.01
Al_2O_3	18.09	18.44	18.30	19.07	18.24	18.02	17.90	18.21	18.36
FeO_{tot}	29.20	30.47	28.99	29.04	29.15	29.02	27.79	27.68	27.37
MnO	1.22	1.04	1.19	1.12	1.07	1.11	0.59	0.39	0.53
MgO	13.01	12.64	13.36	12.90	13.79	13.18	14.31	14.55	14.29
CaO	0.02	0.01	0.01	0.03	0.00	0.06	0.12	0.04	0.12
Na_2O	0.03	0.07	0.12	0.13	0.05	0.07	0.10	0.02	0.01
K_2O	0.04	0.02	0.00	0.01	0.01	0.01	0.04	0.00	0.03
Sum	88.35	89.17	88.90	88.75	89.32	88.11	88.39	88.11	88.36
28 oxygens									
Si	5.739	5.658	5.727	5.638	5.717	5.727	5.830	5.773	5.825
Al	4.578	4.649	4.593	4.795	4.554	4.569	4.474	4.556	4.572
Ti	0.000	0.001	0.000	0.000	0.000	0.003	0.000	0.003	0.001
Fe^{3+}	0.021	0.000	0.005	0.015	0.000	0.003	0.053	0.057	0.120
Fe^{2+}	5.218	5.468	5.154	5.159	5.173	5.216	4.866	4.852	4.703
Mn	0.222	0.188	0.214	0.202	0.192	0.202	0.106	0.070	0.095
Mg	4.162	4.024	4.236	4.096	4.351	4.223	4.515	4.598	4.489
Ca	0.004	0.001	0.003	0.007	0.001	0.014	0.027	0.008	0.027
Na	0.027	0.060	0.095	0.106	0.044	0.058	0.079	0.013	0.007
K	0.020	0.011	0.002	0.004	0.003	0.005	0.019	0.000	0.017
X_{Fe}	0.56	0.58	0.55	0.56	0.54	0.55	0.52	0.52	0.52
Fe^{3+}/Al	0.005	0.000	0.001	0.003	0.000	0.001	0.012	0.013	0.026

Table 3. Representative Na-amphibole analyses.

	Gln-I					Gln-II					
SiO_2	56.48	56.31	57.19	57.34	56.34	56.49	56.89	56.66	56.16	56.12	56.09
TiO_2	0.07	0.00	0.09	0.04	0.07	0.05	0.05	0.05	0.02	0.02	0.04
Al_2O_3	9.54	9.69	10.88	9.32	9.33	8.96	10.02	8.70	10.19	9.17	10.49
FeO_{tot}	13.95	13.35	13.80	14.41	13.89	13.32	13.93	13.65	13.35	13.44	13.83
MnO	0.04	0.11	0.15	0.04	0.04	0.07	0.04	0.15	0.00	0.22	0.04
MgO	8.63	8.92	8.25	8.63	8.52	10.72	10.22	11.02	10.86	10.72	10.35
CaO	0.36	0.38	0.44	0.33	0.39	0.23	0.22	0.22	0.16	0.27	0.23
Na_2O	7.11	7.94	6.78	6.94	7.22	6.76	5.45	5.62	6.28	6.28	6.11
K_2O	0.01	0.01	0.01	0.03	0.01	0.01	0.01	0.01	0.00	0.01	0.01
Sum	96.19	96.71	97.59	97.08	95.81	96.61	96.83	96.08	97.02	96.25	97.19
13 cations											
T:Si	7.95	7.93	7.91	7.99	7.98	7.79	7.73	7.76	7.64	7.73	7.63
$Al^{(IV)}$	0.05	0.07	0.09	0.01	0.02	0.21	0.27	0.24	0.36	0.27	0.37
T-Sum	8.00	8.00	8.00	8.00	8.00	8.00	8.00	8.00	8.00	8.00	8.00
$C:Al^{(VI)}$	1.53	1.54	1.68	1.52	1.54	1.25	1.34	1.16	1.28	1.22	1.32
Ti	0.01	0.00	0.01	0.00	0.01	0.01	0.01	0.01	0.00	0.00	0.00
Fe^{3+}	0.45	0.24	0.45	0.50	0.36	1.07	1.42	1.51	1.37	1.28	1.36
Mg	1.81	1.87	1.70	1.79	1.80	2.20	2.07	2.25	2.20	2.20	2.10
Fe^{2+}	1.19	1.33	1.15	1.18	1.29	0.46	0.16	0.06	0.14	0.27	0.22
Mn	0.00	0.01	0.02	0.00	0.00	0.01	0.00	0.02	0.00	0.03	0.00
C-Sum	5.00	5.00	5.00	5.00	5.00	5.00	5.00	5.00	5.00	5.00	5.00
B:Ca	0.05	0.06	0.07	0.05	0.06	0.03	0.03	0.03	0.02	0.04	0.03
Na	1.94	1.94	1.82	1.87	1.94	1.81	1.44	1.49	1.66	1.68	1.61
B-Sum	1.99	2.00	1.88	1.92	2.00	1.84	1.47	1.52	1.68	1.72	1.65
A:Ca	0.00	0.00	0.00	0.00	0.00	0.00	0.00	0.00	0.00	0.00	0.00
Na	0.00	0.23	0.00	0.00	0.04	0.00	0.00	0.00	0.00	0.00	0.00
K	0.00	0.00	0.00	0.01	0.00	0.00	0.00	0.00	0.00	0.00	0.00
A-Sum	0.00	0.23	0.00	0.01	0.04	0.00	0.00	0.00	0.00	0.00	0.00
X_{Mg}	0.52	0.54	0.52	0.52	0.52	0.59	0.57	0.59	0.59	0.59	0.57
Fe^{3+}/Al	0.28	0.15	0.25	0.33	0.23	0.74	0.88	1.07	0.84	0.86	0.81
	Gln-II			Gln-III							
SiO_2	56.23	56.43	56.64	56.37	55.75	56.16	56.53	55.71	56.68	56.38	
TiO_2	0.02	0.04	0.00	0.00	0.00	0.00	0.01	0.00	0.00	0.02	
Al_2O_3	9.32	9.18	9.43	7.76	8.04	7.39	6.97	9.40	8.08	8.24	
FeO_{tot}	13.93	14.13	14.41	14.91	15.14	15.72	16.09	15.02	16.01	16.10	
MnO	0.04	0.15	0.07	0.02	0.03	0.04	0.09	0.11	0.11	0.00	
MgO	10.72	10.20	10.03	10.01	10.01	9.72	9.66	9.49	9.69	9.81	
CaO	0.19	0.23	0.22	1.01	0.99	1.31	0.88	0.48	1.17	1.09	
Na_2O	5.95	6.02	5.45	6.59	6.41	6.51	6.62	6.28	5.45	5.62	

Table 3. (Continued).

K_2O	0.01	0.01	0.01	0.02	0.02	0.04	0.03	0.01	0.01	0.00	
Sum	96.41	96.39	96.26	97.27	96.38	96.90	96.87	96.50	97.2	97.3	
13 cations											
T:Si	7.70	7.77	7.77	7.89	7.81	7.89	7.93	7.74	7.83	7.78	
$Al^{(IV)}$	0.30	0.23	0.23	0.11	0.19	0.11	0.07	0.26	0.17	0.22	
T-Sum	8.00	8.00	8.00	8.00	8.00	8.00	8.00	8.00	8.00	8.00	
$C:Al^{(VI)}$	1.21	1.26	1.29	1.17	1.13	1.11	1.08	1.28	1.14	1.12	
Ti	0.00	0.00	0.00	0.00	0.00	0.00	0.00	0.00	0.00	0.00	
Fe^{3+}	1.45	1.29	1.43	0.85	1.02	0.82	0.91	1.15	1.22	1.27	
Mg	2.19	2.09	2.05	2.09	2.09	2.04	2.02	1.96	1.99	2.02	
Fe^{2+}	0.15	0.34	0.22	0.89	0.76	1.02	0.97	0.60	0.63	0.59	
Mn	0.00	0.02	0.01	0.00	0.00	0.00	0.01	0.01	0.01	0.00	
C-Sum	5.00	5.00	5.00	5.00	5.00	5.00	5.00	5.00	5.00	5.00	
B:Ca	0.03	0.03	0.03	0.15	0.15	0.20	0.13	0.07	0.17	0.16	
Na	1.58	1.61	1.45	1.79	1.74	1.77	1.80	1.69	1.46	1.50	
B-Sum	1.61	1.64	1.48	1.94	1.89	1.97	1.93	1.76	1.63	1.66	
A:Ca	0.00	0.00	0.00	0.00	0.00	0.00	0.00	0.00	0.00	0.00	
Na	0.00	0.00	0.00	0.00	0.00	0.00	0.00	0.00	0.00	0.00	
K	0.00	0.00	0.00	0.00	0.00	0.01	0.01	0.00	0.00	0.00	
A-Sum	0.00	0.00	0.00	0.00	0.00	0.01	0.01	0.00	0.00	0.00	
X_{Mg}	0.58	0.56	0.55	0.54	0.54	0.52	0.52	0.53	0.52	0.52	
Fe^{3+}/Al	0.96	0.86	0.94	0.67	0.77	0.67	0.79	0.75	0.93	0.94	

abbreviations in this paper followed those of Whitney and Evans (2010).

Figure 2 gives a schematic illustration of the textural contexts of minerals during the prograde and retrograde stages in the studied sample. Based on the textural relationships and mineral composition, the prograde mineral assemblage can be divided into 2 stages: assemblage-I and assemblage-II. Assemblage-I consists of garnet-I (core), clinopyroxene-I, Na-amphibole-I, chlorite-I, phengite-I, epidote-I, rutile, and quartz (Figure 3a). Garnet-II (rim), clinopyroxene-II, Na-amphibole-II, phengite-II, epidote-II, lawsonite-I, and rutile are minerals of assemblage-II (Figure 3a). Assemblage-I, the first paragenesis of the prograde stage, was only observed as inclusions in the garnet cores (garnet-I). The predominant inclusion minerals in the garnet core were chlorite-I and glaucophane-I, respectively. Assemblage-II, representing peak metamorphic conditions, was observed in the groundmass and as inclusions in the garnet rims (garnet-II). Parallel alignment of lawsonite-I, epidote-II, glaucophane-II, and omphacite-II defined a pronounced lineation and foliation (Figure 3b). The retrograde stage was defined by the appearance of chlorite-II. This mineral was not in equilibrium with assemblage-II. Garnet porphyroblasts consisting of resorbed garnet-I and garnet-II that subsequently crystallized on it, were partly or completely replaced by chlorite-II along the cracks during the retrograde stage (Figure 3c). In this stage, chlorite-II, after garnet, was the preferred site for lawsonite-II and epidote-III crystallization (Figure 3h). In addition, a texturally darker edge part (glaucophane-III) on matrix glaucophane (glaucophane-II) is a common further retrograde stage mineral. Garnet corresponding to ca. 21% of modal volume occurred as porphyroblast up to 2 mm in diameter. It shows textural and chemical zonation. In the core, garnet-I contains clinopyroxene-I, Na-amphibole-I, chlorite-I, phengite-I, epidote-I, rutile, and quartz inclusions. Garnet-I has commonly anhedral crystal boundaries. A resorption zone between garnet-I and garnet-II was represented by Sps peaks (Figures 4a and 4b). The range of composition for garnet-I and-II can be given as $Alm_{61-64}Prp_{9-13}Grs_{21-24}Sps_{3-6}$ and $Alm_{64-66}Prp_{5-8}Grs_{25-26}Sps_{2-5}$, respectively (Table 1). Garnet-I had a higher Prp end-member composition than garnet-II, but was poorer in Grs and Alm (Figure 4b). Garnet-I showed a typical prograde compositional zoning characterized by a bell-shaped Sps pattern (Figure 4a). Alm, Prp, and $X_{Mg}(Mg/Mg+Fe_{(tot)}=0.13–0.17)$ increased from the core to resorbed boundary. Grs displays fluctuation in the range of 21–24 mol% in garnet-I (Figure 4a). Stoichiometric calculation pointed to the fact that garnet-I did not contain Fe^{3+} (Table 1). However, the Fe^{3+} value increased in the resorption zone and garnet-II (0.01 p.f.u.; Table 1). Garnet-II, from the resorption zone to the rim (Figure

Table 4. Representative epidote analyses.

	Ep-I								Ep-II		
SiO_2	37.68	37.51	37.13	37.52	37.85	37.89	37.74	37.95	37.87	38.27	37.94
TiO_2	0.11	0.01	0.07	0.05	0.11	0.11	0.17	0.07	0.06	0.14	0.09
Al_2O_3	22.81	20.90	21.34	20.74	22.82	22.87	22.90	22.93	25.61	25.24	25.44
Fe_2O_3	14.19	16.19	15.47	16.48	14.33	14.50	14.53	14.22	10.45	10.85	11.15
MnO	0.33	0.41	0.46	0.45	0.42	0.41	0.14	0.34	0.07	0.40	0.09
MgO	0.00	0.00	0.00	0.00	0.00	0.02	0.01	0.00	0.07	0.02	0.07
CaO	22.38	22.13	22.96	22.44	22.46	22.51	22.73	22.73	23.56	22.77	23.56
Na_2O	0.02	0.02	0.03	0.00	0.00	0.00	0.01	0.02	0.02	0.00	0.03
K_2O	0.00	0.00	0.00	0.01	0.01	0.00	0.00	0.00	0.01	0.00	0.01
Sum	97.52	97.16	97.47	97.69	98.00	98.32	98.24	98.25	97.73	97.70	98.36
12.5 oxygens											
Si	3.02	3.04	3.00	3.03	3.02	3.01	3.00	3.02	2.99	3.02	2.98
Al	2.15	2.00	2.03	1.97	2.14	2.14	2.15	2.15	2.38	2.35	2.36
Fe^{3+}	0.86	0.99	0.94	1.00	0.86	0.87	0.87	0.85	0.62	0.64	0.66
Ti	0.01	0.00	0.00	0.00	0.01	0.01	0.01	0.00	0.00	0.01	0.01
Mg	0.00	0.00	0.00	0.00	0.00	0.00	0.00	0.00	0.01	0.00	0.01
Mn	0.02	0.03	0.03	0.03	0.03	0.03	0.01	0.02	0.00	0.03	0.01
Ca	1.92	1.92	1.99	1.94	1.92	1.92	1.94	1.94	1.99	1.93	1.98
Ps(%)	28	33	32	33	29	29	29	28	21	22	22
Fe^{3+}/Al	0.40	0.49	0.46	0.51	0.40	0.40	0.41	0.40	0.26	0.27	0.28
	Ep-II						Ep-III				
SiO_2	37.99	38.31	38.22	38.21	37.65	38.12	37.63	37.68	36.31	38.18	38.00
TiO_2	0.04	0.09	0.06	0.10	0.04	0.05	0.05	0.02	0.09	0.10	0.10
Al_2O_3	24.99	25.17	24.93	24.87	24.07	24.27	23.37	23.86	23.62	23.74	23.37
Fe_2O_3	11.38	11.88	12.22	12.12	12.14	12.12	12.60	13.06	12.79	13.49	13.95
MnO	0.26	0.08	0.02	0.07	0.27	0.28	0.27	0.32	0.22	0.46	0.13
MgO	0.04	0.08	0.08	0.04	0.02	0.01	0.02	0.00	0.03	0.02	0.01
CaO	23.62	22.84	22.78	22.75	23.57	23.48	23.11	23.29	22.95	22.48	22.18
Na_2O	0.03	0.01	0.02	0.00	0.01	0.00	0.04	0.03	0.01	0.01	0.00
K_2O	0.01	0.00	0.00	0.00	0.00	0.00	0.01	0.00	0.01	0.00	0.00
Sum	98.35	98.45	98.33	98.16	97.77	98.32	97.09	98.26	96.03	98.46	97.76
12.5 oxygens											
Si	2.99	3.01	3.01	3.01	3.00	3.01	3.02	2.99	2.95	3.02	3.02
Al	2.32	2.33	2.31	2.31	2.26	2.26	2.21	2.23	2.26	2.21	2.19
Fe^{3+}	0.67	0.70	0.72	0.72	0.73	0.72	0.76	0.78	0.78	0.80	0.84
Ti	0.00	0.01	0.00	0.01	0.00	0.00	0.00	0.00	0.01	0.01	0.01
Mg	0.00	0.01	0.01	0.00	0.00	0.00	0.00	0.00	0.00	0.00	0.00
Mn	0.02	0.01	0.00	0.00	0.02	0.02	0.02	0.02	0.02	0.03	0.01
Ca	1.99	1.92	1.92	1.92	2.01	1.99	1.99	1.98	2.00	1.90	1.89
Ps(%)	23	23	24	24	24	24	26	26	26	26	28
Fe^{3+}/Al	0.29	0.30	0.31	0.31	0.32	0.32	0.34	0.35	0.35	0.36	0.38

Table 5. Representative lawsonite analyses.

	Lws-I								Lws-II		
SiO_2	38.38	38.46	38.86	38.78	38.48	39.96	38.46	38.29	39.43	39.33	37.95
TiO_2	0.09	0.08	0.06	0.05	0.11	0.10	0.10	0.06	0.08	0.10	0.16
Al_2O_3	30.64	30.60	29.82	30.37	30.59	29.96	30.62	30.50	30.80	30.64	30.52
FeO_{tot}	1.52	1.54	1.39	1.42	1.47	1.47	1.46	1.61	1.95	1.77	1.92
MnO	0.02	0.00	0.00	0.02	0.02	0.02	0.00	0.01	0.00	0.05	0.02
MgO	0.00	0.00	0.01	0.00	0.00	0.02	0.02	0.02	0.00	0.01	0.02
CaO	17.03	16.97	17.33	16.92	17.01	16.83	17.03	17.05	17.23	16.92	16.81
Na_2O	0.00	0.00	0.00	0.01	0.00	0.02	0.01	0.02	0.00	0.00	0.01
K_2O	0.01	0.00	0.00	0.00	0.00	0.00	0.00	0.00	0.01	0.00	0.00
Sum	87.68	87.65	87.46	87.56	87.68	88.37	87.69	87.56	89.49	88.81	87.40
12.5 oxygens											
Si	3.18	3.18	3.22	3.21	3.18	3.27	3.18	3.17	3.20	3.21	3.16
Al	2.99	2.98	2.92	2.96	2.98	2.89	2.99	2.98	2.94	2.95	2.99
Fe^{3+}	0.09	0.10	0.09	0.09	0.09	0.09	0.09	0.10	0.12	0.11	0.12
Fe^{2+}	0.02	0.03	0.01	0.01	0.03	0.01	0.01	0.02	0.03	0.00	0.02
Ti	0.01	0.01	0.00	0.00	0.01	0.01	0.01	0.00	0.00	0.01	0.01
Mg	0.00	0.00	0.00	0.00	0.00	0.00	0.00	0.00	0.00	0.00	0.00
Mn	0.00	0.00	0.00	0.00	0.00	0.00	0.00	0.00	0.00	0.00	0.00
Ca	1.51	1.50	1.54	1.50	1.51	1.48	1.51	1.52	1.50	1.48	1.50
Fe^{3+}/Al	0.032	0.032	0.030	0.030	0.031	0.031	0.030	0.034	0.040	0.037	0.040

4b), included clinopyroxene-II, Na-amphibole-II, epidote-II, and lawsonite and showed a prograde growth zoning with increasing Prp, Alm, and decreasing Grs and Sps end-members (Figures 4a and 4b). In garnet-II, the reversed zoning of Sps was limited or inexistent.

Chlorite-I, brunsvigite, (Figure 5a), formed the dominant inclusion phase in garnet-I (Figure 4b). The X_{Fe} (=$Fe^{(tot)}$/$Fe^{(tot)}$+Mg) content of chlorite-I ranged from 0.54 to 0.58 (Figure 5b; Table 2). The Fe^{3+} content, calculated assuming full site occupancy, was estimated as 0.005–0.021 p.f.u. MnO ranged from 1.04 to 1.22 wt.%. The X_{Fe} of chlorite-II (brunsvigite; Figure 5a) was lower than that for chlorite-I and varied from 0.516 to 0.521 (Table 2). The Fe^{3+} and Fe^{3+}/Al contents of chlorite-II ranged from 0.053 to 0.120 p.f.u. and 0.012 to 0.026, respectively.

Na-amphibole, defining the main foliation with omphacite, corresponded to ca. 31% of the modal volume (Figure 3b). Although all of the Na-amphiboles were plotted in the glaucophane field (Leake et al., 1997) (Figure 6a; Table 3), considering the textural relationships and chemical composition, they can be divided into 2 groups, where both glaucophane-I and glaucophane-II were products of the prograde stages (Figures 2 and 6b). Retrograde zonation of glaucophane-II from the rim to core was recognized as glaucophane-III (Figure 3d). Glaucophane-I (X_{Mg}: 0.52-0.54) occurred as randomly disturbed inclusions in garnet-I. In this group, the $Ca^{(B)}$ ranged from 0.05 to 0.07 p.f.u. and Fe^{3+}/Al was up to 0.33. Glaucophane-II was observed both in the matrix, as prismatic individual crystals, and as inclusions in garnet-II (Figure 2). Glaucophane-II, occurring in the matrix, had lower $Ca^{(B)}$(0.02–0.04 p.f.u) than that of glaucophane-III (0.07–0.20 p.f.u). The Fe^{3+}/Al values of glaucophane-II and III were 0.74–1.07 and 0.67–0.94, respectively (Figure 6b; Table 3). The $Fe^{(tot)}$ content of glaucophane-II was 1.55 p.f.u. It was up to 1.85 p.f.u. in glaucophane-III (Figure 6c). Glaucophane-II, occurring in garnet-II, had a homogeneous composition identical to that of the core composition of glaucophane-II occurring in the matrix.

Epidote occurred both as inclusions in the garnet and in the matrix, and formed ca. 12% of the modal volume. The Ps composition of epidote-I, occurring as inclusions in garnet-I, ranged from 28 to 33 (Table 4). The Fe^{3+}/Al contents were in the range of 40–51. Epidote-II occurred both in the matrix and as inclusions in garnet-II. Epidote-II crystals in the matrix commonly contained euhedral glaucophane-II, omphacite-II, and phengite-II inclusions. Epidotes in the matrix showed retrograde zoning with

Table 6. Representative clinopyroxene analyses.

	Cpx-I			Cpx-II					
SiO_2	54.34	54.38	54.04	53.88	54.95	54.89	53.65	53.96	53.85
TiO_2	0.00	0.02	0.04	0.04	0.05	0.05	0.03	0.04	0.06
Al_2O_3	3.59	3.53	4.04	4.87	5.93	6.10	5.61	6.04	6.22
FeO_{tot}	12.48	13.14	12.06	13.97	11.88	12.51	13.39	12.03	12.33
MnO	0.01	0.00	0.06	0.02	0.07	0.00	0.02	0.00	0.03
MgO	8.95	8.83	8.79	7.47	7.16	6.94	7.25	7.79	7.33
CaO	15.45	14.91	14.57	12.54	12.45	12.06	12.17	13.19	12.46
Na_2O	5.76	5.91	7.03	7.01	7.16	7.33	6.94	6.45	6.99
K_2O	0.00	0.00	0.00	0.01	0.00	0.00	0.04	0.01	0.00
Cr_2O_3	0.00	0.00	0.00	0.00	0.01	0.00	0.00	0.00	0.00
Sum	100.58	100.72	100.62	99.81	99.66	99.98	99.10	99.52	99.26
4 cations									
Si	1.97	1.97	1.94	1.97	2.00	2.00	1.97	1.97	1.97
Al^{IV}	0.03	0.03	0.06	0.03	0.00	0.00	0.03	0.03	0.03
Al^{VI}	0.13	0.13	0.11	0.18	0.25	0.26	0.21	0.23	0.24
Fe^{2+}	0.08	0.08	-0.07	0.08	0.11	0.12	0.10	0.12	0.09
Fe^{3+}	0.30	0.31	0.43	0.35	0.25	0.26	0.31	0.25	0.29
Mg	0.48	0.47	0.47	0.39	0.38	0.36	0.37	0.40	0.38
Ti	0.00	0.00	0.00	0.00	0.00	0.00	0.00	0.00	0.00
Cr	0.00	0.00	0.00	0.00	0.00	0.00	0.00	0.00	0.00
Na	0.41	0.42	0.49	0.50	0.51	0.52	0.49	0.46	0.50
Ca	0.60	0.58	0.56	0.49	0.49	0.47	0.48	0.52	0.49
Mg	0.00	0.00	0.00	0.01	0.01	0.01	0.02	0.03	0.02
Quad	59	58	50	49	49	48	50	54	50
Jd	12	12	10	17	26	26	21	22	23
Ae	29	30	40	34	25	26	30	24	28
X_{Mg}	0.56	0.54	0.57	0.48	0.51	0.49	0.48	0.52	0.50
	Cpx-II				Cpx-II				
SiO_2	53.97	53.86	53.86	54.46	53.97	53.86	53.86	54.46	
TiO_2	0.01	0.05	0.03	0.00	0.01	0.05	0.03	0.00	
Al_2O_3	6.27	6.24	6.73	5.64	6.27	6.24	6.73	5.64	
FeO_{tot}	12.35	12.40	12.45	12.39	12.35	12.40	12.45	12.39	
MnO	0.04	0.00	0.09	0.00	0.04	0.00	0.09	0.00	
MgO	7.42	7.29	7.09	7.61	7.42	7.29	7.09	7.61	
CaO	12.52	12.51	12.25	12.96	12.52	12.51	12.25	12.96	
Na_2O	6.81	6.81	6.91	6.27	6.81	6.81	6.91	6.27	
K_2O	0.01	0.01	0.01	0.00	0.01	0.01	0.01	0.00	
Cr_2O_3	0.00	0.00	0.00	0.02	0.00	0.00	0.00	0.02	
Sum	99.40	99.16	99.41	99.34	99.40	99.16	99.41	99.34	
4 cations									
Si	1.97	1.97	1.97	2.00	1.97	1.97	1.97	2.00	
Al^{IV}	0.03	0.03	0.03	0.00	0.03	0.03	0.03	0.00	

Table 6. (Continued).

Al^{VI}	0.24	0.24	0.26	0.24	0.24	0.24	0.26	0.24	
Fe^{2+}	0.11	0.12	0.12	0.18	0.11	0.12	0.12	0.18	
Fe^{3+}	0.27	0.26	0.26	0.20	0.27	0.26	0.26	0.20	
Mg	0.38	0.37	0.36	0.37	0.38	0.37	0.36	0.37	
Ti	0.00	0.00	0.00	0.00	0.00	0.00	0.00	0.00	
Cr	0.00	0.00	0.00	0.00	0.00	0.00	0.00	0.00	
Na	0.48	0.48	0.49	0.45	0.48	0.48	0.49	0.45	
Ca	0.49	0.49	0.48	0.51	0.49	0.49	0.48	0.51	
Mg	0.03	0.02	0.03	0.04	0.03	0.02	0.03	0.04	
Quad	51	51	50	55	51	51	50	55	
Jd	23	24	25	24	23	24	25	24	
Ae	26	25	25	20	26	25	25	20	
X_{Mg}	0.50	0.50	0.49	0.50	0.50	0.50	0.49	0.50	

Table 7. Representative white mica analyses.

	Ph-I			Ph-II					
SiO_2	49.49	49.51	49.30	52.20	51.91	51.97	52.03	51.80	51.69
TiO_2	0.01	0.01	0.02	0.09	0.24	0.20	0.18	0.18	0.17
Al_2O_3	26.10	26.64	26.89	22.85	23.47	23.18	23.62	22.45	23.73
FeO_{tot}	6.20	5.84	6.34	5.05	4.83	4.83	4.89	5.08	5.25
MnO	0.01	0.01	0.00	0.04	0.00	0.01	0.02	0.03	0.00
MgO	2.98	3.05	3.08	3.96	3.86	4.10	4.18	4.17	4.17
CaO	0.08	0.06	0.02	0.10	0.03	0.00	0.02	0.03	0.04
Na_2O	0.05	0.10	0.05	0.09	0.16	0.14	0.14	0.14	0.15
K_2O	10.89	10.80	11.03	10.24	10.90	11.09	10.91	10.84	10.69
Sum	95.80	96.01	96.72	94.62	95.40	95.51	95.99	94.71	95.89
11 oxygens									
Si	3.36	3.35	3.32	3.55	3.51	3.52	3.50	3.54	3.48
Ti	0.00	0.00	0.00	0.00	0.01	0.01	0.01	0.01	0.01
Al	2.09	2.12	2.14	1.83	1.87	1.85	1.87	1.81	1.89
Fe	0.35	0.33	0.36	0.29	0.27	0.27	0.27	0.29	0.30
Mn	0.00	0.00	0.00	0.00	0.00	0.00	0.00	0.00	0.00
Mg	0.30	0.31	0.31	0.40	0.39	0.41	0.42	0.42	0.42
Ca	0.01	0.00	0.00	0.01	0.00	0.00	0.00	0.00	0.00
Na	0.01	0.01	0.01	0.01	0.02	0.02	0.02	0.02	0.02
K	0.94	0.93	0.95	0.89	0.94	0.96	0.94	0.94	0.92
Ms	0.61	0.62	0.65	0.43	0.44	0.43	0.45	0.41	0.47
Cel	0.38	0.36	0.34	0.56	0.54	0.55	0.53	0.57	0.51
Prg	0.01	0.02	0.01	0.01	0.02	0.02	0.02	0.02	0.02
X_{Mg}	0.46	0.48	0.46	0.58	0.59	0.60	0.60	0.59	0.59

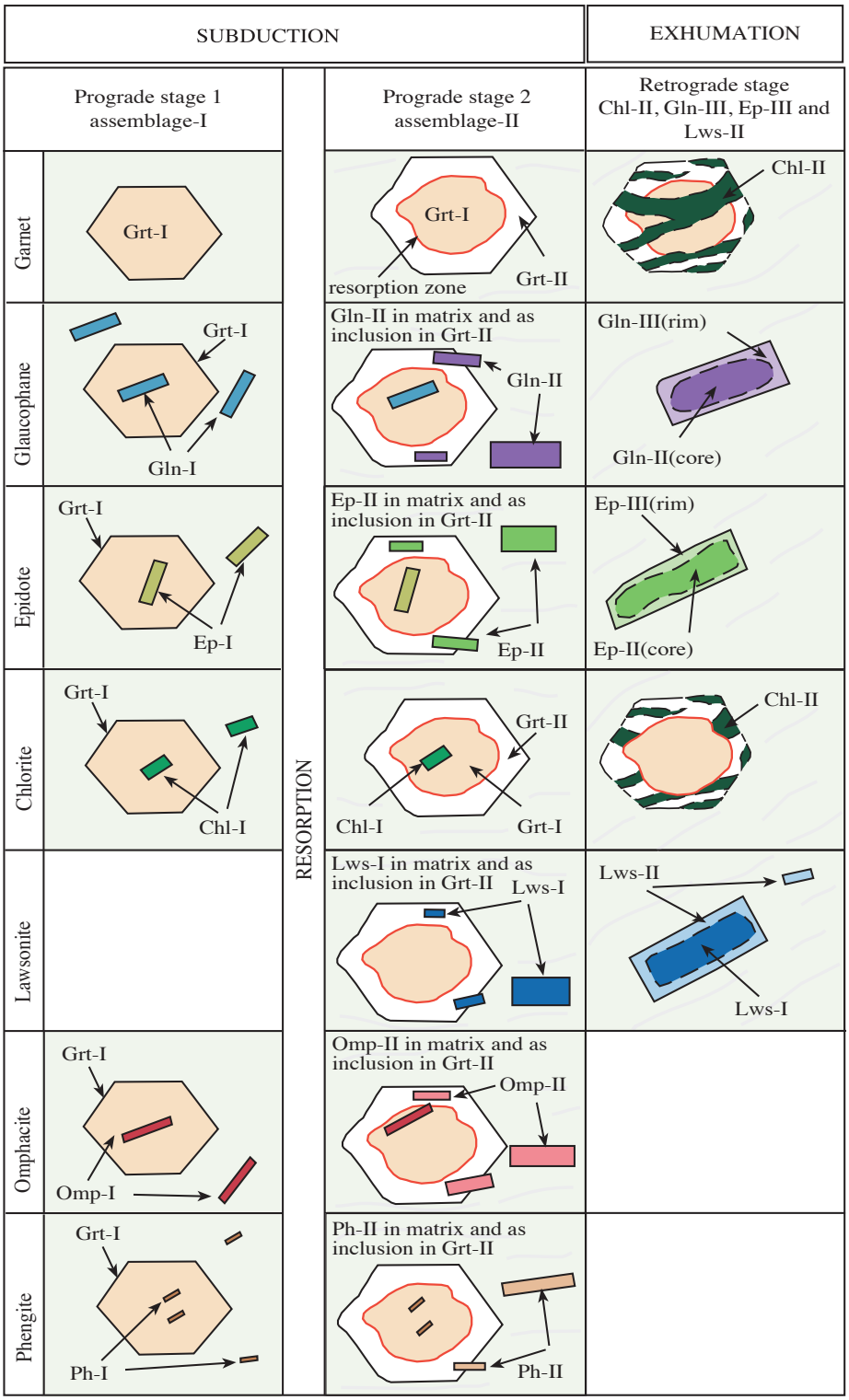

Figure 2. Textural relationships of the minerals during the prograde and retrograde stages.

decreasing Al content from the core (2.38 p.f.u.) to the rim (2.19 p.f.u.) (Figure 3e).The Al-rich part (core) of these epidotes was defined as epidote-II, with the Al-poor part (rim) as epidote-III (Figure 3e). In the core and rims, the Ps content ranged from 21–24 to 26–28 vol.%, respectively. In the core, the Fe^{3+}/Al content was lower (0.26–0.32) than

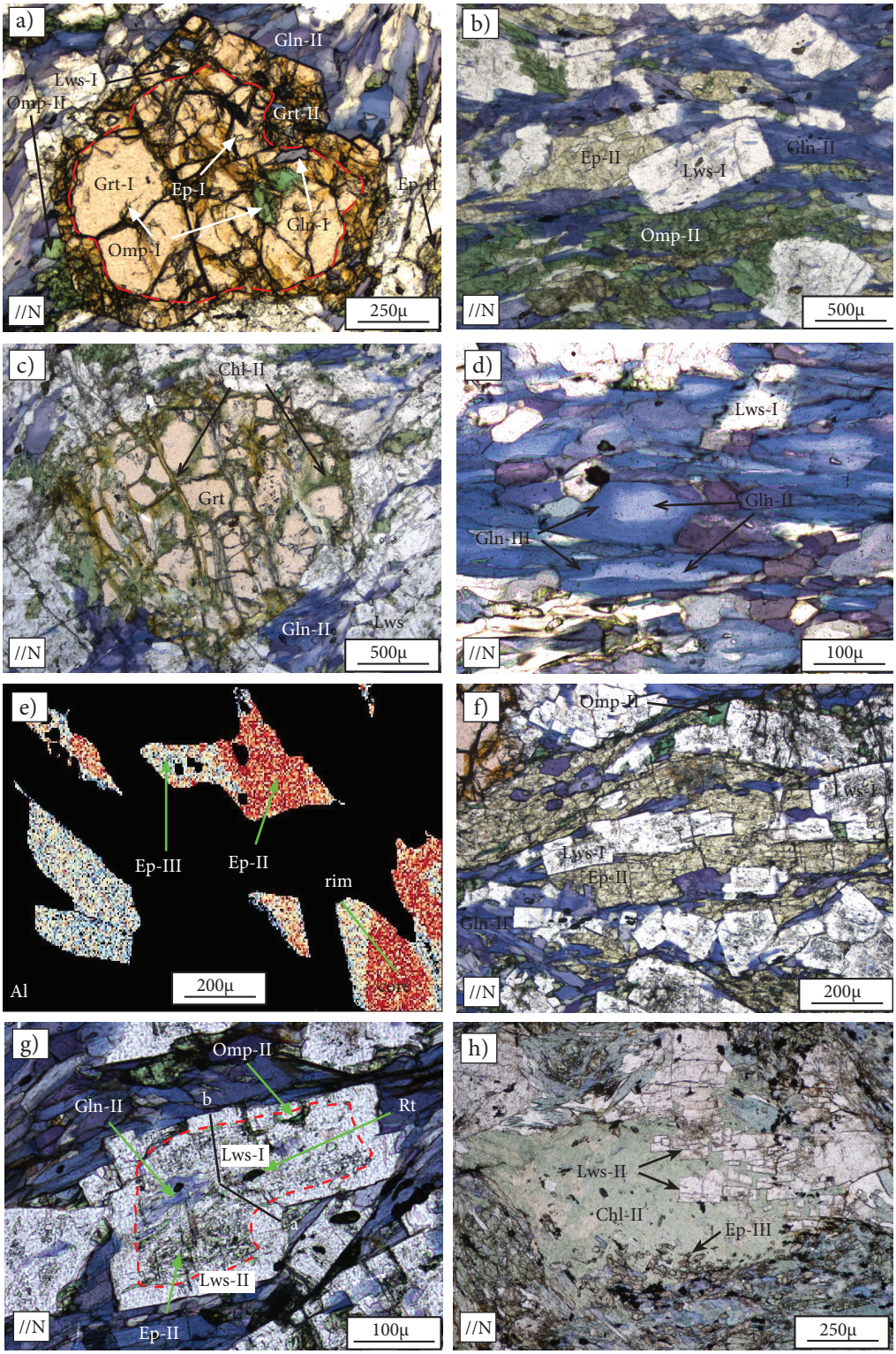

Figure 3. a) Inclusions of Gln, Omp, Ep, and Lws in garnet showing 2 growth stages. The red stippled line marks the resorption boundary between Grt-I and Grt-II; b) alignment of tabular shaped high-pressure minerals in the matrix; c) replacement of garnet by Chl-II along the cracks; d) zoning of Gln-II from core to rim; e) Al zonation of Ep-II from core to rim in the Al map (XMapTools). Hot colors represent higher concentration; f) Lws-II and Ep-II equilibrium of assemblage-II. Coexisting Lws-II and-Ep-II show sharp crystal boundaries in the matrix; g) zoning of lawsonite with inclusions of Gln-II, Omp-II, Ep-II, and rutile in the core. The rim is relatively inclusion free; and h) euhedral lawsonite-II belonging to the retrograde stage in a chlorite-II domain.

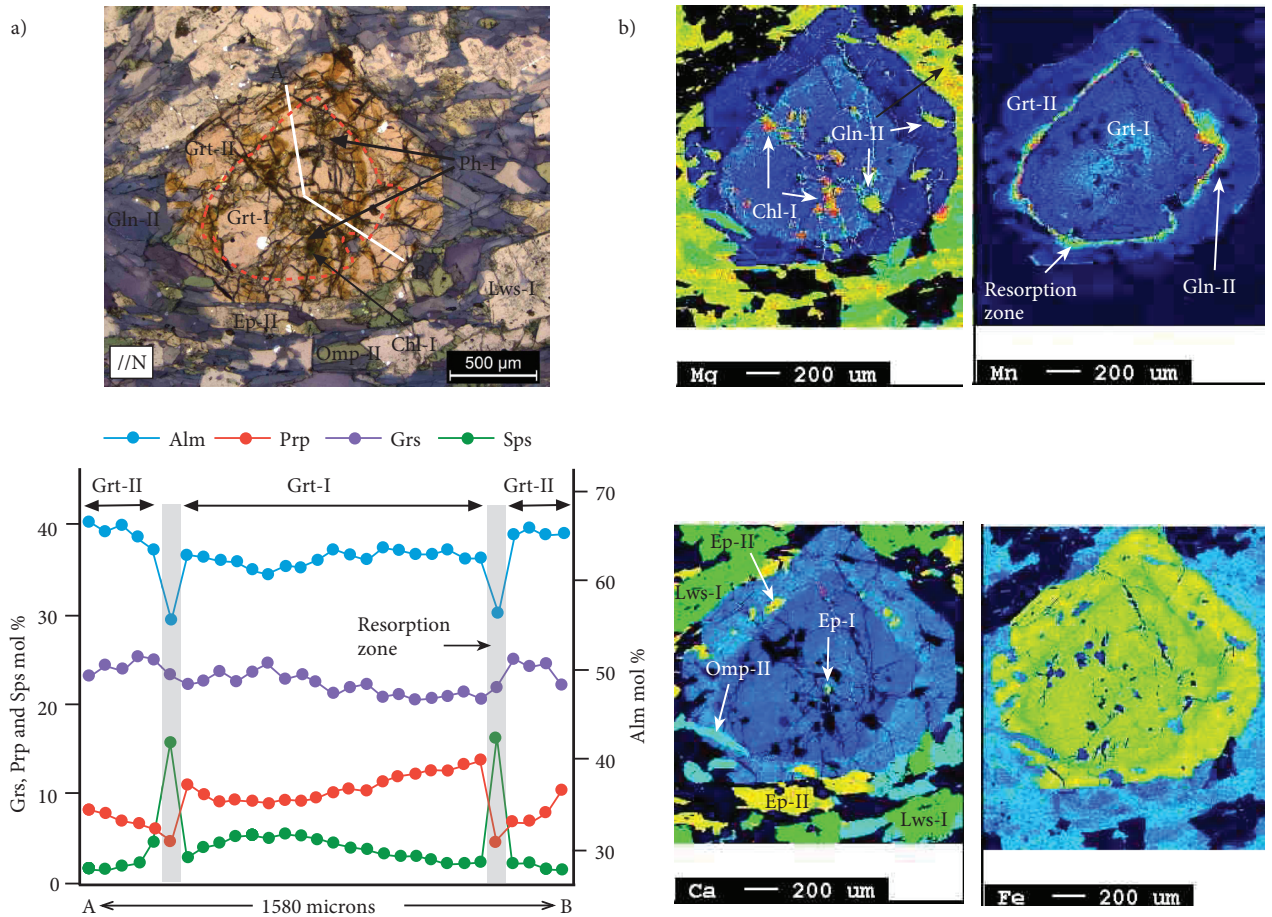

Figure 4. a) Garnet with end-member compositions (white line: compositional profile), b) X-ray element maps for Mg, Mn, Ca, and Fe. Hot colors represent higher concentration.

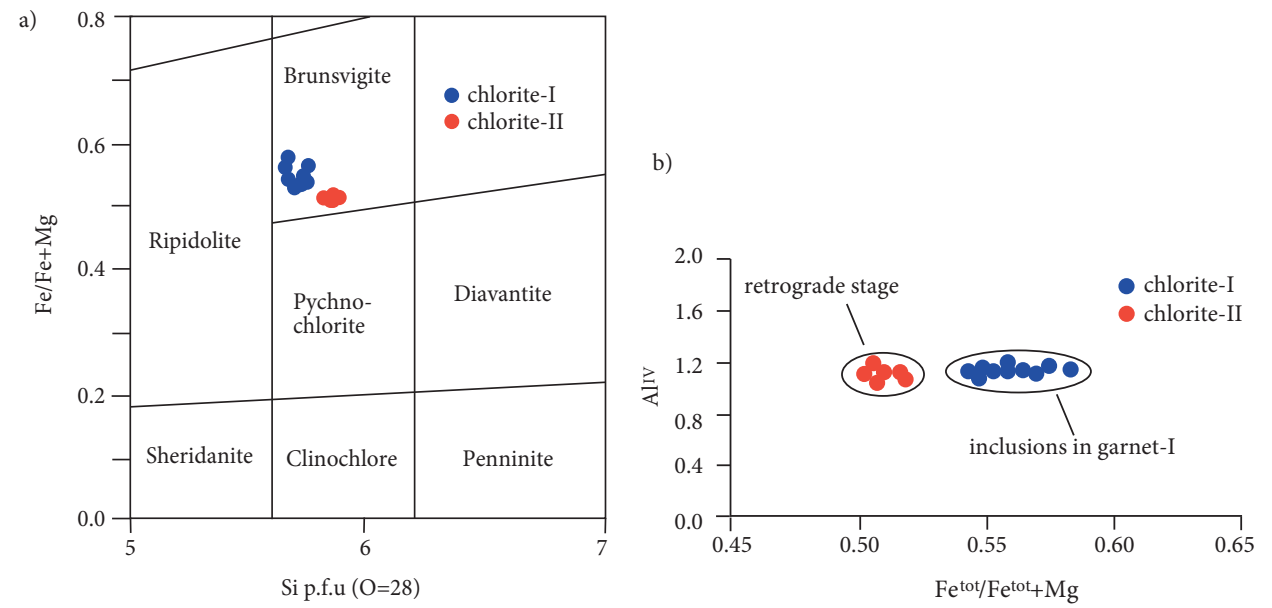

Figure 5. a) Chemical compositions of chlorites plotted in a Hey (1954) diagram, and b) compositional variations of chlorite in terms of $Fe^{(tot)}/Fe^{(tot)}+Mg$ vs. Al^{IV}.

in the rim (0.34–0.38) (Figure 6d). The sharp contacts, free of any reaction evidence, between lawsonite-I and epidote-II in the matrix, indicated textural equilibrium (Figure 3f). Epidote-II inclusions in garnet-II and the core composition of epidote-II in the matrix had similar Ps content (21–24 vol.%).

Euhedral lawsonite porphyroblasts, ca. 24 vol.%, showed textural and chemical zoning that developed during the prograde and retrograde stages (Figure 2). This textural zonation of lawsonite was defined by inclusion-rich cores (lawsonite-I) with glaucophane-II, omphacite-II, epidote-II, and rutile inclusions (prograde stage) and inclusion-free rims or rims bearing tiny/cloudy inclusions (lawsonite-II; retrograde stage) (Figure 3g). In addition, epidote-III and euhedral-individual lawsonite-II were also observed in the chlorite-II domain after garnet (Figure 3h). A pronounced chemical zonation was characterized by increased $FeO^{(tot)}$ from the core (lawsonite-I) (1.39 vol.%) to the rim (lawsonite-II) (1.95 vol.%) (Table 5). The Fe^{3+}/Al ratio changed from 0.030–0.032 in the core to 0.040 in the rim (Figures 3g and 6e). Lawsonite-I contained rare epidote-I inclusions. The diffusive character of the boundaries between these 2 phases can be interpreted as a textural signature of the replacement of epidote-I by lawsonite during the prograde stage.

Subhedral prismatic clinopyroxene crystals, making up ca. 8 vol.% of the matrix, showed parallel alignment to the foliation (Figure 3b). Based on the textural and compositional evidence, 2 types of clinopyroxene could be distinguished. Clinopyroxene-I ($Jd_{10-12}\,Ae_{29-40}\,Q_{50-59}$ mol%), occurring as inclusions in garnet-I (Figure 3a), was plotted in the aegirine-augite field of the Morimoto et al., (1988) diagram (Figure 6f). Its X_{Mg} ranged between 0.54 and 0.57 (Table 6). Clinopyroxene-II, observed both in the matrix and as inclusions in garnet-II, had similar end-member compositions ($Jd_{21-26}Ae_{20-29}Q_{46-55}$). It was plotted in the omphacite and aegirine-augite fields (Figure 6f). The X_{Mg} of clinopyroxene-II ranged between 0.48 and 0.52.

The modal volume % of phengitic white mica (Figure 6g) was ca. 3%. Texturally, 2 generations of white micas developed during the prograde stage; phengite-I and phengite-II. Phengite-I was only observed as small inclusion crystals (50–60 microns) in garnet-I (Figure 4a). The Si^{4+} and X_{Mg} values were 3.32–3.36 p.f.u. and 0.46–0.48, respectively (Table 7). In general, phengite-II was observed in epidote-II-rich domains. In contrast to phengite-II, phengite-I was rich-in $Al^{(tot)}$ and poor-in Mg (Table 7).The compositional range of phengite-II,occurring in garnet-II and the matrix, can be given as Si^{4+}=3.48-3.55p.f.u. and X_{Mg}=0.58–0.60. Some phengite-II grains showed slight compositional zonation characterized by $Fe^{(tot)}$-poor (0.27–0.28 p.f.u) cores and $Fe^{(tot)}$-rich (0.29–0.30 p.f.u) rims (Figure 6h).

4. Equilibrium paragenesis and P–T conditions

4.1. Garnet growth stages

The computer program, GRTMOD, using natural compositional records (Lanari et al., 2017) was applied to model the growth stages of the garnet. Considering the resorption and/or fractionation of previously crystallized garnet, GRTMOD optimizes a new local effective bulk composition for each garnet growth stage (Lanari et al., 2017). The internally consistent thermodynamic database JUN92.bs (Berman, 1988, and subsequent updates) was selected for the GRTMOD modeling. The compositions of the growth zones were characterized by standardized X-ray element maps using the software XMapTools (Lanari et al., 2014c). In addition, GRTMOD interacts with Theriak (de Capitani and Brown, 1987) uses the extension Theriak_D (Duesterhoeftand de Capitani, 2013). Gibbs free-energy minimizations were performed using Theriak-Domino. The Theriak_D add-on for the Theriak-Domino software package supports testing the stability of mineral phases along any P–T path and P–T grid or calculating the solid rock density (Duesterhoeft and de Capitani, 2013). Bulk composition used for calculation represented the rock sample analyzed by X-ray fluorescence spectroscopy at Potsdam University (Table 8). In the calculations, the Co (cost function value) was lower than STOL (=0.1) (tolerance to select the result as a solution) in all of the optimization stages of GRTMOD. Based on the quantitative X-ray compositional maps of the end-members, the growth of garnet during the prograde P–T history can be divided into 2 stages, represented by a resorption boundary (Figure 7a). At the rims of the garnet, the effects of intracrystalline diffusion were not observed or were restricted to the outermost narrow rims (<~10 microns). The garnet core composition ($Alm_{59}Prp_{14}Grs_{21}Sps_5$),measured using XMapTools, and the bulk rock composition applied to the model for first-stage garnet growth (garnet-I) predicted P–T conditions of 12.6 kbar/495°C and a garnet modal volume of 16.6 ± 2.8%. The garnet-II composition ($Alm_{61}Prp_{10}Grs_{25}Sps_4$), calculated using XMapTools, and the estimated garnet-I P–T conditions and modal vol. % were used to model the second growth zoning of the garnet (garnet-II). This modeling yielded an optimized local effective bulk composition (Table 8), a modal volume % (10.9 ± 1.8), and P–T conditions (16.9 kbar/511 °C) for garnet-II. After resorption, the estimated modal volume for garnet-I was calculated as 10.2 vol.% (Figure 7b; Table 9). The model implied that 38.5 vol.% of previously formed garnet (garnet-I) was resorbed. The total garnet modal volume % in the matrix was 21.1%. The rock density, which was 3.25 gr/cm^2 in the first stage, was 3.29 gr/cm^2 in the second garnet growth stage.

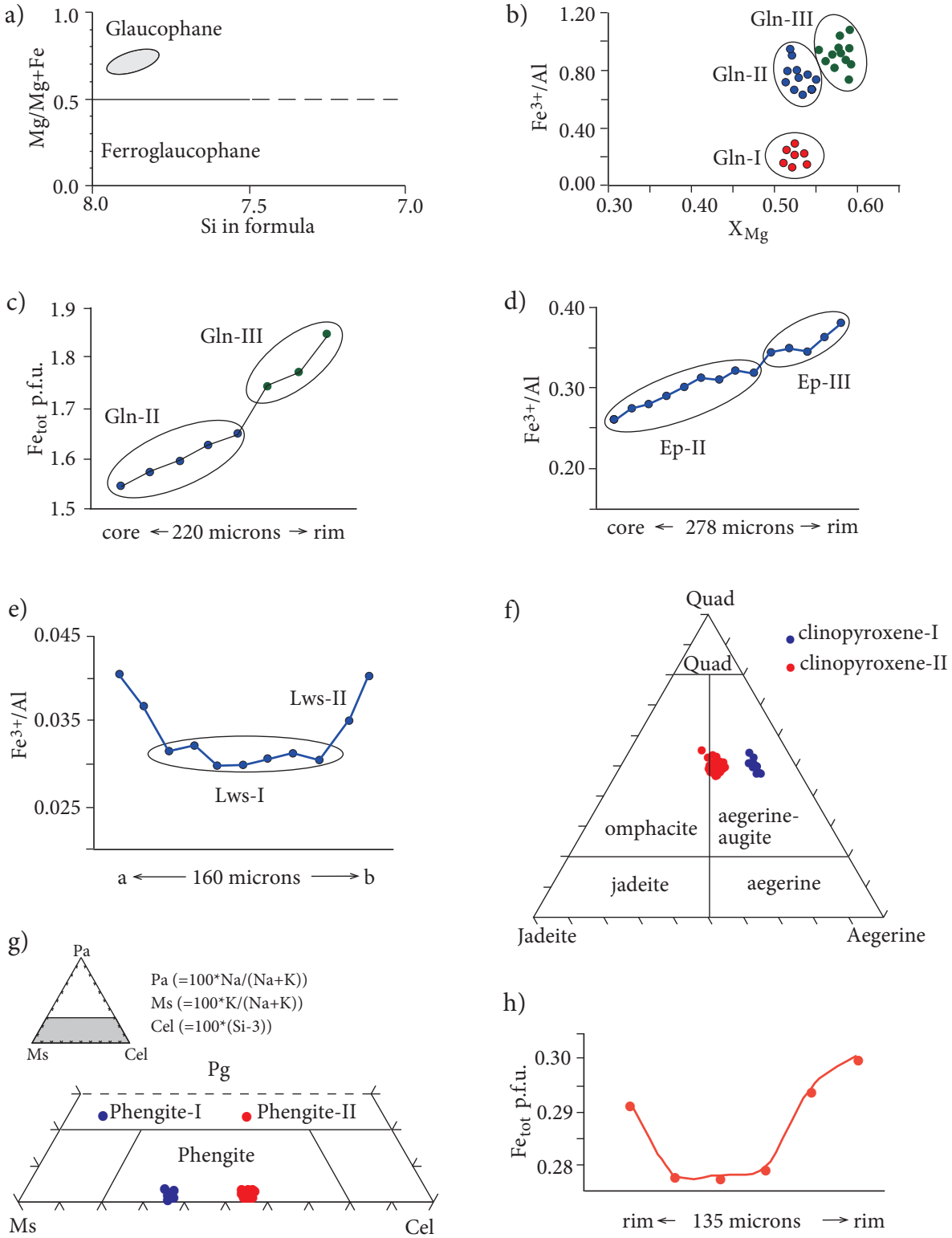

Figure 6. a) Chemical compositions of Na-amphiboles plotted on the classification diagram of Leake et al. (1997); b) compositional variations of Na-amphiboles in terms of $Fe^{3+}/Al^{(tot)}$ vs. X_{Mg}; c) variation of $Fe^{(tot)}$ p.f.u. from core to rim in Na-amphibole-II; d) Fe^{3+}/Al variation from core to rim in Epidote-II; e) Fe^{3+}/Al variation from rim to rim in lawsonite; f) clinopyroxene-I and clinopyroxene-II compositions on the Na-clinopyroxene discrimination diagram of Morimoto et al., (1988); g) compositional distribution of phengite-I and -II in a Pg-Ms-Cel triangle; and h) $Fe^{(tot)}$ zonation in phengite-II grain.

Table 8. Compositions used for the modeling calculations and modal volume of the minerals in the thin section.

	Bulk composition	Effective bulk composition	Minerals*	vol.%
SiO_2	45.35	46.92	Garnet	21
TiO_2	0.64	0.70	Omphacite	8
Al_2O_3	19.02	18.78	Epidote	12
FeO_{tot}	11.93	9.36	Glaucophane	31
MnO	0.24	0.06	Lawsonite	24
MgO	4.02	4.10	Phengite	3
CaO	11.81	12.51	Chlorite	1
Na_2O	2.58	2.98	Sum	100
K_2O	0.30	0.34		
H_2O	3.93	4.25		
Sum	99.82	100.00		

*Minerals less than 1vol.% were not taken into account.

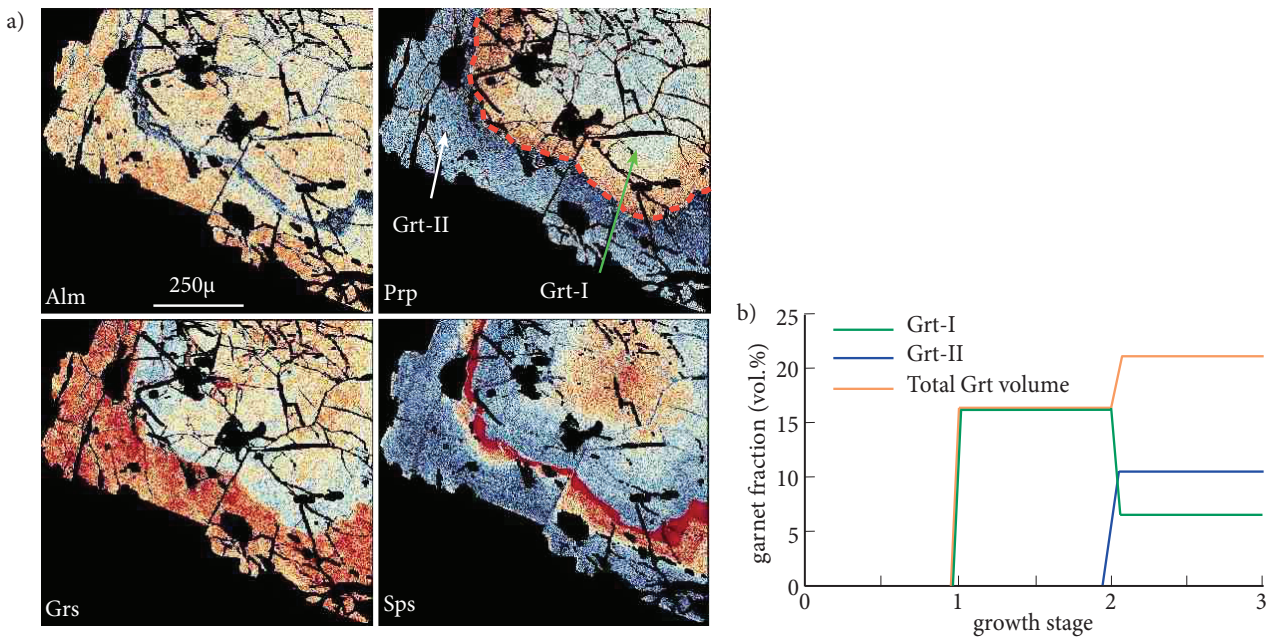

Figure 7. a) Compositional map data of garnet end-members (Alm, Prp, Grs, and Sps) obtained using XMapTools, and b) volume fraction of garnet predicted during growth stages.

4.2. Phase diagrams

The modeling of the P–T path was performed using the phase-diagram calculation software package Theriak-Domino (de Capitani, 1994; de Capitani and Petrakakis, 2010) and the thermodynamic database and accurate mineral solution models of Berman (1988, updated). The sample (M04-420) was modeled in the system Na_2O–CaO–K_2O–FeO–MgO–Al_2O_3–SiO_2–H_2O (NCKFMASH). Because the solid solution models for the Fe^{3+}-silicates are not very accurate, Fe_2O_3 was not included in the system. All Fe was considered as Fe^{2+}. The Ti and Mn were excluded to simplify the system. Thermodynamic data on Mn in silicates other than garnet is not very accurate; hence, it was not attempted to include Mn. Cross-cutting

Table 9. Summary of the results obtained by GRTMOD modeling.

Garnet resorption (vol.%)			
	Grt-I	Grt-II	Total
Prograde stage 1	0.0	0.0	0.0
Prograde stage 2	4.60	0.0	4.60
Volume of garnet (vol.%)			
	Grt-I	Grt-II	Total
Prograde stage 1	16.60	0.0	16.60
Prograde stage 2	10.20	10.90	21.10
Newly grown garnet (vol.%)			
	Grt-I	Grt-II	Total
Prograde stage 1	16.60	0.0	16.60
Prograde stage 2	0.0	10.90	10.90
Rock density (g/ccm)			
	density		
Prograde stage 1	3.25		
Prograde stage 2	3.29		

veins that included prograde or retrograde minerals did not exist in the sample. The existence of many hydrous phases (chlorite, glaucophane, epidote, white mica), and especially lawsonite, showed that water remained in excess and was rather pure from burial to peak conditions. Therefore, aH_2O was assumed as 1. Calcite was absent in the mineral assemblage of the sample. For this reason, CO_2 was not considered as a component in the phase diagram calculations. The bulk rock, effective bulk compositions, and thin section mineral vol.% are given in Table 8.

The bulk rock composition of the sample was used for the construction of the phase diagram for assemblage-I. In assemblage-I, chlorite-I, epidote-I, and garnet-I were of special interest in order to determine the equilibrium field bounded by lawsonite and feldspar stability fields (Figure 8a). The distribution of chlorite-I inclusions in garnet-I (Figure 4b) showed that growth of garnet probably occurred in a chlorite equilibrium field. This modeling indicated that the modal vol.% of chlorite-I, in equilibrium with garnet-I, could be up to 6 vol.%. Clinopyroxene-I (Jd:10–12), phengite-I (Si^{4+}:3.32–3.36 p.f.u.), and chlorite-I (X_{Fe}=0.54–0.58) isopleths yielded P–T conditions of 12±1 kbar and 485 ± 10 °C for assemblage-I (Figure 8b). The amount of resorption of the garnet may have caused significant changes in the effective composition (Lanari et al., 2017). For the following prograde stage, represented by assemblage-II (Figure 8c), an optimized local effective bulk composition (Table 8) using GRTMOD was computed by subtracting of the amount of garnet-I produced during first garnet growth stage from the bulk rock composition.

The X_{Mg} value of the new garnet generation (garnet-II), which was free of chlorite inclusion, increased from the inner (0.08) to the outer (0.11) part of the rim. At the inner rim of garnet-II, the P–T conditions of were estimated as 15 ± 0.5 kbar and 490 ± 10°C using glaucophane-II (inclusion) X_{Mg} (0.55) and garnet-II X_{Mg}(0.08) compositions. Whereas, at the outer rim of garnet-II, the P–T conditions reached peak metamorphic conditions, represented by the garnet + lawsonite + epidote + glaucophane + omphacite + phengite + H_2O stability field. It was calculated as 17 ± 1.0 kbar and 515 ± 10°C using garnet X_{Mg}(0.11), glaucophane-II $X_{Mg\text{-}core}$ (0.59), and phengite-II X_{Mg} (0.58–0.60) isopleths (Figure 8d).

One of the post-peak minerals was chlorite-II,which showed progressive growth at the expense of garnet during the retrograde stage. X_{Fe} isopleths (0.51–0.52) of chlorite-II after garnet were located in the lawsonite-epidote equilibrium field. This yielded P–T conditions ca. 8 kbar and 365 ± 10°C for the retrograde stage (Figures 9a and 9b).

5. Discussion

5.1. Factors controlling epidote–lawsonite coexistence

The epidote–lawsonite boundary in the blueschist/eclogite facies diagrams is represented either by a univariant line or a quite narrow transition zone, in which both minerals can occur as stable phases. The lawsonite–epidote transition in Figure 9 occupies a closed stability field. The width of this field was strongly controlled by 1) the ferric iron proportion of minerals (fO_2) (Evans, 1989; Lopez-Carmona et al., 2013), 2) H_2O availability (Clark et al., 2006; Tsujimori and Ernst, 2014), and 3) the X_{CO2} content of the fluid phase (Poli et al., 2009; Goto et al., 2017).

Ferric iron content may significantly affect the phase relationships during metamorphism (e.g., Diener and Powell, 2010). A high-oxidation state stabilizes epidote and the position of the lawsonite–epidote phase boundary shifts to higher pressures at elevated values of fO_2 (e.g., Warren and Waters, 2006; Lopez-Carmona et al., 2013). However, Fe^{2+} and Mg were treated as a single component, because variation in the Fe^{2+}/Mg ratio had little effect on the stability of phases in the diagram (Brown, 1977), whereas varying Fe^{3+}/Al ratios among the phases affected precisely the P–T conditions (Evans, 1990). The computed phase diagrams showed that iron-free pairs, such as zoisite/clinozoisite–glaucophane, did not possess a closed stability field in the P–T diagram (Evans, 1990). It was reported by Davis and Whitney (2006, 2008) that epidote, omphacite, phengite, and glaucophane included a significant amount of Fe^{3+}in the Sivrihisar area. As mentioned by Davis and Whitney (2006), lawsonite and epidote were in equilibrium with the matrix assemblage-II. Calculations of these equilibria indicated

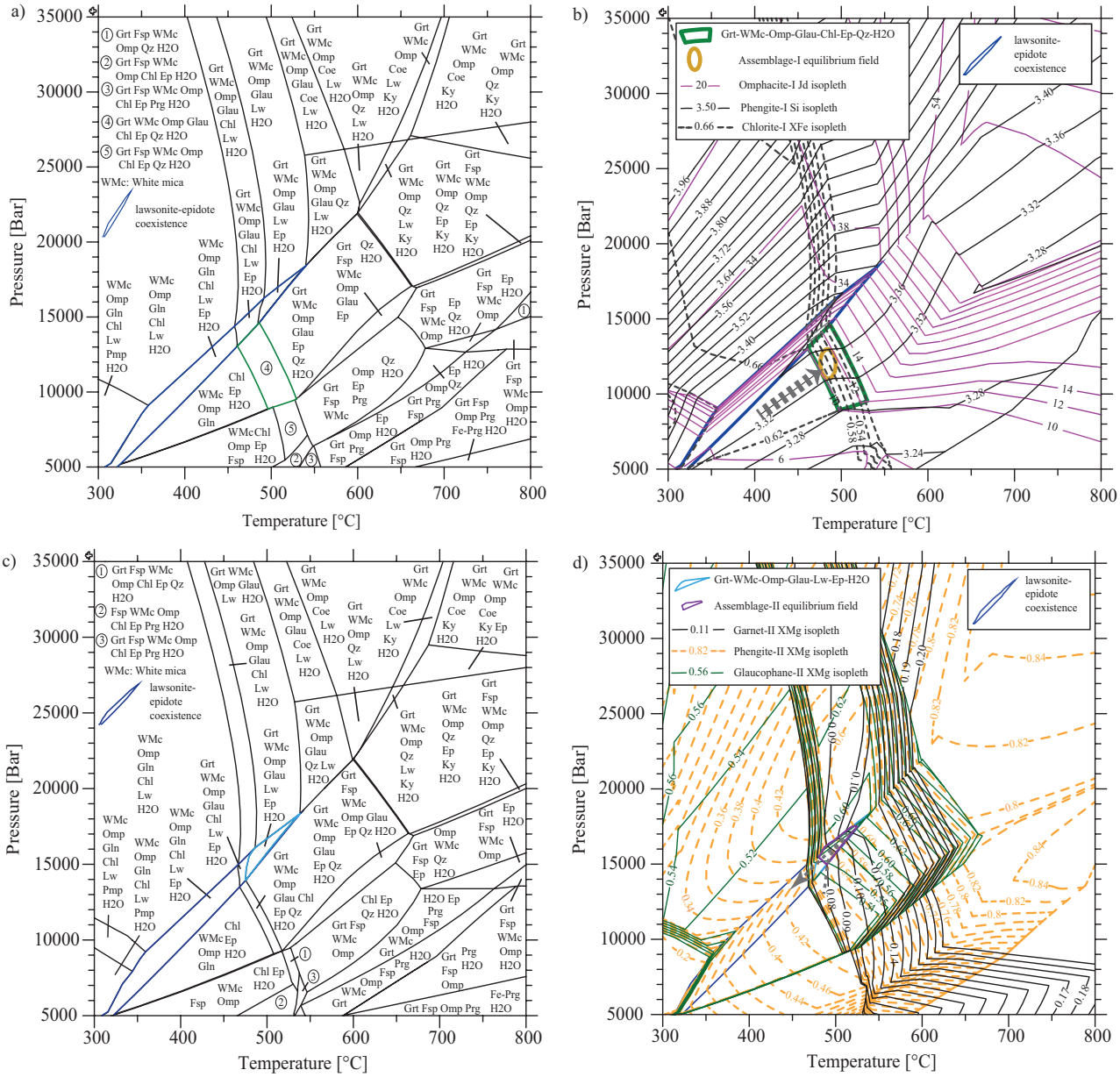

Figure 8. a) Phase diagram showing equilibrium assemblages, calculated in the NCKFMASH system for bulk composition at aH_2O = 1; b) equilibrium conditions for assemblage-I: isopleths calculated with omphacite-I, phengite-I, and chlorite-I; c) phase diagram showing equilibrium assemblages, calculated in the NCKFMASH system for effective bulk composition at aH_2O = 1; and d) equilibrium conditions for assemblage-II: isopleths calculated with garnet-II, phengite-II, and glaucophane-II.

that phase compatibilities were sensitive to small differences in the phase composition, especially the Fe^{3+}/A1 ratio. The stability field widened as a function of the increase of the Fe^{3+}/A1 ratio in the minerals (Evans, 1990). Contrarily, the epidote-bearing blueschist field decreased in size as the ratio Fe^{2+}/Mg increased (Evans, 1990). In the current sample, epidote, glaucophane, phengite and lawsonite occurring in the matrix displayed Fe zonation from the core to rim (Figure 6). Similarly, the Fe^{3+}/A1 ratios of these minerals increased towards the rims in the lawsonite-epidote equilibrium field (Tables 3–5 and 7).This increase in Fe^{3+} in the rims can be interpreted as related to an increase in oxygen activity during exhumation. In addition, a partial decrease in temperature during exhumation promoted the incorporation of Fe^{3+} in epidote (Poli and Schmidt, 2004).

Bulk-rock composition and water content are expected to play an important role in the crystallization and preservation of lawsonite (Clarke et al., 2006).

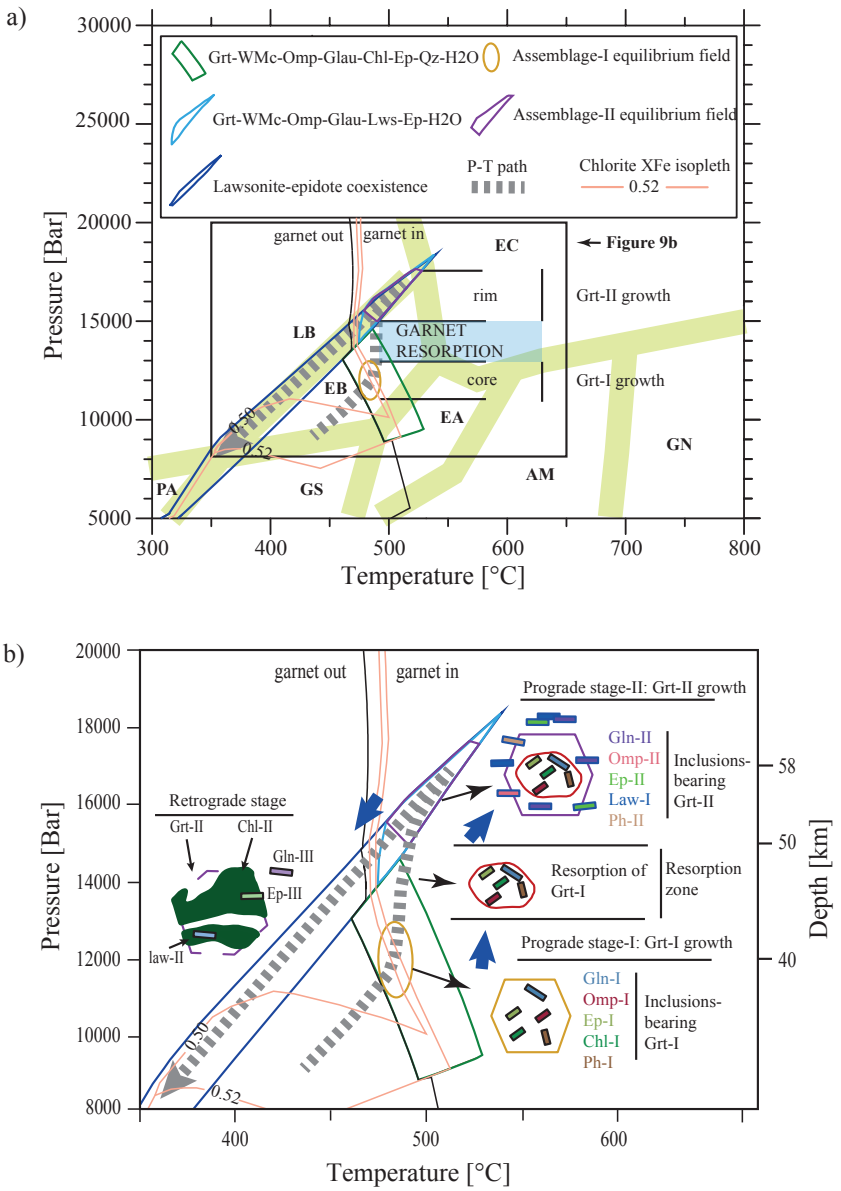

Figure 9. a) Prograde and retrograde P–T evolution obtained from bulk and effective bulk composition. Metamorphic facies boundaries are after Bucher and Frey (2002). Metamorphic facies abbreviations: AM, amphibolite facies; EA, epidote-amphibolite facies; EB, epidote-blueschist facies; EC, eclogite facies; GN, granulite facies; GS, greenschist facies; LB, lawsonite-blueschist facies; PA, pumpellyite actinolite facies. b) P–T path of subduction and exhumation deduced from the observed in garnet (see Figure 2).

Pseudosection modeling and predicted changes in modal mineralogy for the prograde part of the P–T path (Figure 9a) showed that water remained in excess from burial to peak condition. In the studied sample, the inferred pre-peak and peak assemblages comprised >70 vol.% hydrated minerals. Relative vol.% proportions of hydrated assemblages under pre (garnet-I) and peak P–T conditions can be estimated as Chl (6) + Gln (33) + Ep (30) + Ph (3) and Lws (24) + Gln (31) + Ep (12) + Ph (3), respectively. The computed effect of water activity (aH_2O) on the lawsonite-epidote equilibrium field for bulk and effective bulk compositions of the sample is shown in Figures 10a and 10b. Decreasing aH_2O from 1.0 to 0.1 implied a systematic reduction of the extension and displacement of the epidote–lawsonite equilibrium field. Epidote–lawsonite coexistence and their volume % in the matrix can be used as a monitor of aH_2O. Reducing the aH_2O moves the equilibrium field to lower temperature and higher pressure. The locations of a majority of facies boundaries are influenced by aH_2O. This evidence reveals that the boundary between lawsonite and

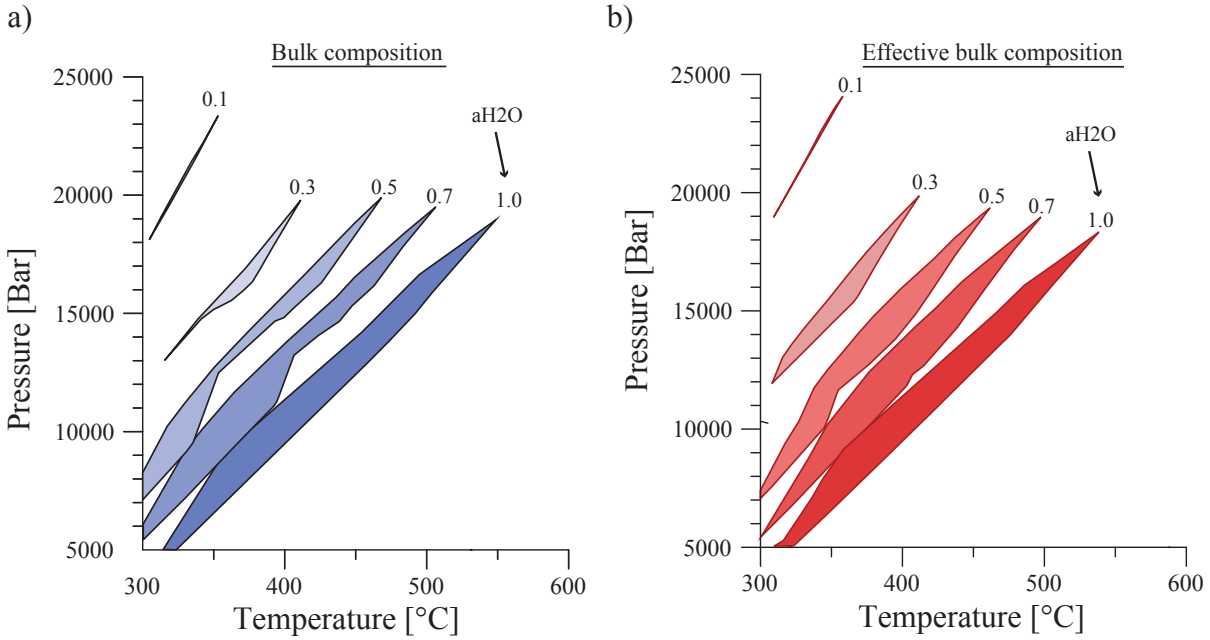

Figure 10. Variation of the epidote–lawsonite equilibrium field as a function of$a$ H_2O for a) bulk and b) effective bulk composition.

epidote transforms from a univariant line to a closed field as a function of increasing aH_2O.

The amount of H_2O in the minerals during the prograde and retrograde stages of metamorphism is illustrated in Figure 11. The chlorite-consuming reaction to form garnet-I released H_2O gradually (Figure 11) and the rock became increasingly denser at ~475–495 °C. Simultaneously, the H_2O contents of the solid phases in the chlorite-consuming P-T region decreased with increasing P–T conditions (Figure 11). In this stage, the inferred H_2O content of the bulk-rock ranged from 2.2 to 2 vol.% and the H_2O content (mol) in the solid phases steeply decreased (Figure 11). A drastic pressure increase (from 12 ± 1 kbar/garnet-I to 15 ±0.5 kbar/garnet-II inner rim and 17 ± 1 kbar/garnet-II outer rim) probably gave rise to resorption of the garnet (Figures 9a and 11).The H_2O content of the solid phases and modal volume of the H_2O for the effective bulk composition during lawsonite-epidote coexistence and garnet-II growth stage were estimated in the range of ca. 5–10 mol and 2–3.6 vol.%, respectively (Figure 11). This pointed to a H_2O infiltration into the rock. As a consequence of high aH_2O, no significant change occurred in the hydrated mineral assemblage of the rock during exhumation within the epidote–lawsonite equilibrium field, except for the replacement of garnet by chlorite (Figure 11). The good preservation of the peak assemblage during the latest stage of exhumation can be attributed to the fact that the H_2O content remained almost constant (Figure 11) .Considering the lack of CO_2 in the bulk rock composition and minerals, it can be suggested that CO_2 had no effect on the epidote–lawsonite equilibrium.

5.2. Effect of effective bulk composition on the phase equilibrium fields

The bulk composition was used to estimate the equilibrium field of assemblage-I. For the equilibrium after garnet resorption, an effective bulk composition, obtained by subtracting the garnet core (garnet-I) composition calculated by GRTMOD from the bulk composition, was used. The major difference of the phase diagram obtained with the effective bulk composition was a narrowing of the equilibrium field of coexisting chlorite and garnet. Nevertheless, the size of the epidote–lawsonite equilibrium field persisted (Figures 8a and 8c).

5.3. Metamorphic history of the blueschist-facies block

During the closure of the northern branch of the Neo-Tethyan Ocean in the Late Cretaceous, the northernmost margin of the Anatolide–Tauride platform, the Tavşanlı Zone, was deeply buried beneath the southward advancing, obducted oceanic lithosphere and the accretionary complex, and underwent HP/LT metamorphism (Okay, 2004). Regarding this tectonic evolution, the Sivrihisar region, located in the Tavşanlı Zone, is a special area where the coexistence of eclogite and blueschist facies metamorphism are observed. In this area, the marbles and overlying blueschists, and eclogitic metabasites, are assumed to represent a coherent sequence, which was deposited on a passive continental margin (Davis and Whitney, 2006). However, the common occurrence of

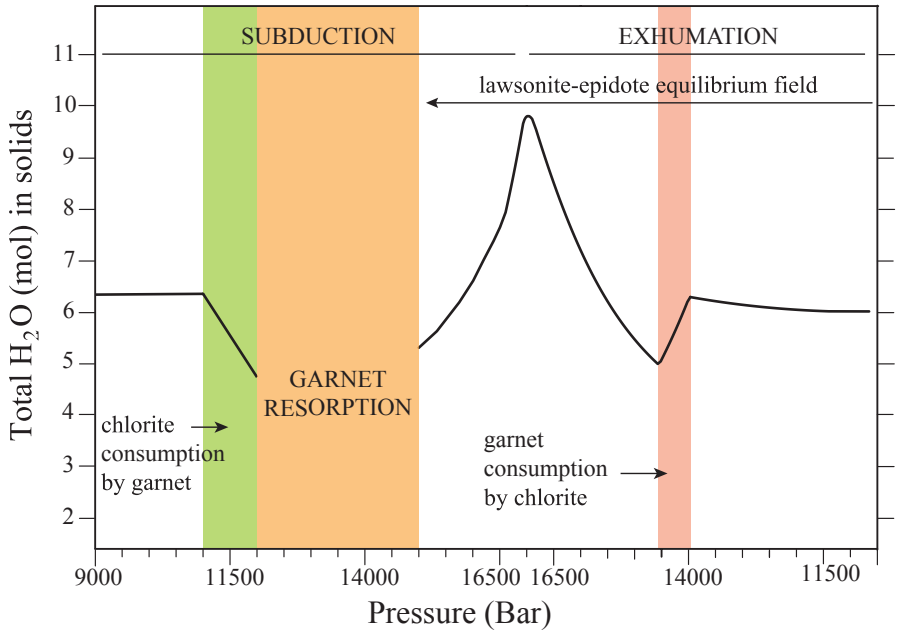

Figure 11. Variation of the total H_2O (mol) in solids as a function of pressure during subduction and exhumation.

the metamorphosed serpentinite lenses in the blueschist-eclogite accretionary complex around Sivrihisar area, as well as over the entire Tavşanlı Zone, precludes the possibilities of primary stratigraphic contact relationships with underlying coherent sequences (Çetinkaplan et al., 2008). The inferred metamorphic evolution of the epidote–lawsonite blueschist sample obtained from combinations of textural relationship, mineral zoning and analytical data is given below.

The prograde stage of the metamorphic evolution was represented by assemblage-I and assemblage-II. Distinctive minerals for assemblage-I were chlorite-I, garnet-I, and epidote-I. This assemblage indicated that the first garnet crystallization with chlorite consumption occurred below the univariant line between lawsonite and epidote. The P–T pseudosection computed from assemblage-I constrained pressure to 12 ± 1 kbar (~40 km) at 485 ± 10°C, suggesting an initial subducting stage under epidote-blueschist facies conditions (Figures 9a and 9b). At that stage, the estimated modal garnet-I vol.% was 16.6 ± 2.8. Microprobe mapping and analyses (Figure 4) showed that prograde compositional zoning in garnet-I was suddenly interrupted, and that garnet-I decreased to from 16.6 to 10.2 vol. % after resorption. The cause of resorption occurring in garnet-I may have been associated with an increase in pressure relative to temperature, as indicated by the lawsonite-bearing and chlorite-free inclusion assemblage (Figure 8c), and increase of jadeite in omphacite inclusions in garnet-II. With the crystallization of garnet-II, the H_2O saturated equilibrium field of assemblage-II (Figure 9b) was reached. The first crystallization of garnet-II occurred at 15 ± 0.5 kbar (~50 km) and 490 ± 10 °C. This P–T condition was estimated by use of an effective bulk composition. The drastic increase of pressure (3 kbar, ~10 km) caused resorption of garnet-I (Figures 9a and 9b).The coexistence of epidote-II–lawsonite-I observed in garnet-II (Figure 9b) and the matrix (Figure 3b) indicated that this crystallization occurred at the lawsonite blueschist/epidote blueschist interface. The peak metamorphic conditions for assemblage-II were determined by the garnet, phengite, and glaucophane isopleths as 17± 1 kbar (~58 km) and 515 ± 10 °C (Figures 8d and 9b). Although it is generally accepted that the Grt + Omp + Lws ± Gln paragenesis defines the lawsonite eclogite facies (Tsujimoriand Ernst, 2014), the calculated peak metamorphic conditions corresponded to the lawsonite blueschist/epidote blueschist interface (Figure 9a). This interface was represented by a stability field of coexisting lawsonite–epidote, as discussed above. The retrograde stage was mainly defined by the existence of chlorite-II after garnet. X_{Fe} isopleths of chlorite-II crossed the lawsonite-epidote equilibrium field in 2 different places (Figures 9a and 9b). Chlorite-II was in equilibrium with garnet at higher-pressure conditions of this stability field (Figures 8c and 9b). However, this situation contradicted the replacement of garnet by chlorite-II in the sample. For this reason, the isopleth of maximum X_{Fe} in chlorite-II, occurring in the lower pressure part of the stability field was considered

to confine the P–T conditions of the retrograde stage (ca. 8 kbar and 365 ± 10 °C) (Figure 9b).Textural evidence indicated that lawsonite was in equilibrium with epidote during the retrograde stage. This suggested that the P–T path followed the lawsonite–epidote stability field during exhumation (Figure 9a).

5.4. Tectonic structure of mafic HP metamorphic rocks in Halilbağı region

Blueschists and eclogites occur along ancient plate boundaries (subduction zones) as coherent tectonic units (Vitale Brovarone et al., 2013) or melanges (accretionary complex) (Agard et al., 2009).The existence of these type rocks in a coherent oceanic unit are inferred to have detached from the descending plate during subduction and accreted to the bottom of the overriding mantle as large tectonic slices (Ruh et al., 2015). The thermal evolution of stratigraphically coherent tectonic units in subduction interfaces can be attained from eclogites and blueschists (Angiboust et al., 2009). The P–T conditions of this evolution are in a certain range (Angiboust et al., 2009). Whereas, accretionary complexes exposed inland may comprise tectonic blocks with contrasting pressure-temperature histories (Pourteau et al., 2019). An accretionary complex may include tectonically juxtaposed HP/LT metamorphosed oceanic (pelagic sedimentary rocks, basalt, gabbro, and ultramafic rocks) and continental rocks. The metamorphic evolution of individual tectonic blocks of HP oceanic rocks in such complexes is different from each other and unique for each block and provide information on the internal dynamics and thermal evolution of subduction channels (Pourteau et al., 2019). The metamorphic evolution of the studied epidote–lawsonite blueschist sample (block) was an individual and specific to the block. The results did not reflect the metamorphic evolution of a particular rock group and accretionary complex. The tectonically juxtaposition of many different types of blocks, the widespread presence of serpentinite blocks among blocks, coexistence of blocks in different ages (ca. 86–104 Ma), and the existence of blocks undergone to different P–T conditions in a small field support the fact that this blocky unit was an accretionary complex (Çetinkaplan et al., 2008; Pourteau et al., 2019). The metamorphic evolution of individual blocks in these types of chaotic complexes records different stages of the evolution of the subduction zone (Hyppolito et al., 2016; Pourteau et al., 2019).

6. Conclusions

- The first stage of the preserved metamorphic evolution for the studied blueschist-facies metabasic block was represented by epidote-blueschist facies at 12 ± 1 kbar (~40 km) and 485 ± 10°C conditions (assemblage-I). In this stage, the reaction of chlorite to garnet was enhanced by dehydration.

- An increase in pressure (3 kbar) triggered resorption of the garnet. This situation caused the garnet modal volume to decrease from 16.6 to 10.2%.

- New garnet crystallization after the resorption event took place under conditions of 15 ± 0.5 kbar (~50 km) and 490 ± 10 °C. Fluid infiltration and an increase in the Fe^{3+}/Al ratio generated favorable conditions for the coexistence of epidote and lawsonite.

-Assemblage-II was characterized by the epidote–lawsonite equilibrium (17 ± 1 kbar (~57 km)/515 ± 10°C) corresponding to the interface separating the lawsonite blueschist and epidote blueschist stability fields.

-Exhumation-related retrogression was limited to the replacement of garnet to chlorite. This reaction increased the H_2O saturation of the rock.

- The exhumation path apparently remained in the epidote–lawsonite equilibrium field.

Acknowledgments

This work was financially supported by D.E.U BAP (04. KB.FEN.066). The author is indebted to Prof. Dr. Osman Candan and Prof. Dr. Roland Oberhänsli for their thoughtful and constructive suggestions. Thanks are extended to Christina Guenter for her assistance with the microprobe at Potsdam University. Also acknowledged is Dr. Michael Bröcker and an anonymous reviewer for their constructive comments, which resulted in an improved manuscript.

References

Agard P, Plunder A, Angiboust S, Bonnet G, Ruh J (2018). The subduction plate interface: rock record and mechanical coupling (from long to short timescales). Lithos 320-321: 537-566.

Agard P, Yamato P, Jolivet L, Burov E (2009). Exhumation of oceanic blueschist sand eclogites in subduction zones: timing and mechanisms. Earth Science Reviews 92: 53-79.

Angiboust S, Agard P, Jolivet L, Beyssac O (2009). The Zermatt-Saas ophiolite: thelargest (60 km wide) and deepest (c. 70-80 km) continuous slice of oceanic lithosphere detached from a subduction zone. Terra Nova 21: 171-180.

Ballevre M, Pitra P, Bohn M (2003). Lawsonite growth in the epidote blueschists from the Ile de Groix (Armorican Massif, France): a potential geobarometer. Journal of Metamorphic Geology 21: 273-735.

Banno S, Sakai C (1989). Geology and metamorphic evolution of the Sanbagawa metamorphic belt, Japan. In: JS Daly, RA Cliff, BWD Yardley (editors). The Evolution of Metamorphic Belts. Oxford, UK: Blackwell Scientific Publications, pp. 519-532.

Bearth P (1973). Gesteins- und Mineralparagenesenaus den Ophiolithen von Zermatt. Schweizerische Mineralogische und Petrographische Mitteilungen 53: 299-334.

Berman RG (1988). Internally consistent thermodynamic data for minerals in the system Na_2O–K_2O–CaO–MgO–FeO–Fe_2O_3–Al_2O_3–SiO_2–TiO_2–H_2O–CO_2. Journal of Petrology 29: 445-522.

Black PM (1977). Regional high-pressure metamorphism in New Caledonia: phase equilibria in the Oue´goadistrict. Tectonophysics 43: 89-107.

Brown EH (1977). Phase equilibria among pumpellyite, lawsonite, epidote and associated minerals in low grade. Contribution Mineralogy of Petrology 64: 123-136.

Bucher K, Frey M (2002). Petrogenesis of Metamorphic Rocks, 7th ed., Springer-Verlag, Berlin: 428 pp (in English).

Candan O, Çetinkaplan M, Oberhänsli R, Rimmele G, Akal C (2005). Alpine high pressure/low temperature metamorphism of Afyon Zone and implication for metamorphic evolution of western Anatolia, Turkey. Lithos 84: 102-124.

Candan O, Dora OÖ, Oberhänsli R, Oelsner F, Dürr S (1997). Blueschist relics in the Mesozoiccoverseries of the Menderes Massif and correlations with Samos Island, Cyclades. Schweizerische Mineralogische und Petrographische Mitteilungen 77: 95-97.

de Capitani C (1994).Gleichgewichtsphasen Diagramme: Theorie und Software. Berichte der Deutschen Mineralogischen Gesellschaft 72 (6): 48.

de Capitani C, Brown TH (1987). The computation of chemical equilibrium in complex systems containing non-ideal solutions. Geochimica et Cosmochimca Acta 51:2639-2652.

de Capitani C, Petrakakis K (2010). The computation of equilibrium assemblage diagrams with Theriak/Domino software. American Mineralogist 95: 1006-1016.

Çetinkaplan M, Candan O, Oberhänsli R, Bousquet R (2008). Pressure–temperature evolution of lawsonite eclogite in Sivrihisar; Tavşanlı Zone–Turkey. Lithos 104:12-32.

Clarke GL, Powell R, Fitzherbert JA (2006). The lawsonite paradox: a comparison of field evidence and mineral equilibria modelling. Journal of Metamorphic Geology 24: 715-725.

Çetinkaplan M, Candan O, Oberhänsli R, Sudo M, Cenki-Tok B (2020). P-T-t evolution of the Cycladic Blueschist Unit in western Anatolia/Turkey: Geodynamic implications for the Aegean region. Journal of Metamorphic Geology 38: 379-419.

Çetinkaplan M, Pourteau A, Candan O, Koralay OE, Oberhänsli R et al. (2016). P-T-t evolution of eclogite / blueschist facies metamorphisminAlanyaMassif:time and space relations with HP event in Bitlis Massif, Turkey. International Journal of Earth Science 105:247-281.

Davis PB (2011). Petrotectonic of lawsonite eclogite exhumation: insights from the Sivrihisar massif, Turkey. Tectonics 30: TC1006.

Davis PB, Whitney DL (2006). Petrogenesis of lawsonite and epidote eclogite and blueschist, Sivrihisar Massif, Turkey. Journal of Metamorphic Geology 24: 823-849.

Davis PB, Whitney DL (2008). Petrogenesis and structural petrology of high-pressure metabasalt pods, Sivrihisar, Turkey. Contribution of Mineralogy and Petrology 156:217-241.

Deiner JFA, Powell R (2010). Influence of ferric iron on the stability of mineral assemblages. Journal of Metamorphic Geology 28: 599-613.

Duesterhoeft E, de Capitani C (2013). Theriak_D: an add-on to implement equilibrium computations in geodynamic models. Geochemical. Geophysic Geosystem 14: 4962-4967.

Enami M, Liou JG, Mattinson CG (2004). Epidote minerals in high P/T metamorphic terranes: subduction zone and high-to ultrahigh pressure metamorphism. Reviews in Mineralogy and Geochemistry 56: 347-398.

Ernst WG (1988). Tectonic history of subduction zones inferred from retrograde blueschist P–T paths. Geology 16:1081–1084.

Ernst WG, Dal Piaz GV (1978). Mineral parageneses of eclogitic rocks and related mafic schists of the piemonte ophiolite nappe, Breuil St-Jacques area, Italian Western Alps. American Mineralogist 63:621-640.

Evans LJ (1989). Chemistry of metal retention by soils. Environment Science and Technology 23:1046-1056.

Evans BW (1990). Phase relations of epidote-blueschists. Lithos 25: 3-23.

Fornash KF, Cosca MA, Whitney DL (2016). Tracking the timing of subduction and exhumation using $^{40}Ar/^{39}Ar$ phengite ages in blueschist- and eclogite-facies rocks (Sivrihisar, Turkey). Contributions to Mineralogy and Petrology 171: 67-86.

Fornash KF, Whitney DL, Seaton NCA (2018). Lawsonite composition and zoning as an archive metamorphic processes in subduction zones. Geosphere 15 (1): 24-46.

Goto D, Morimoto S, Ishidoya S, Aoki S, Nakazawa T (2017). Terrestrial biospheric and oceanic CO_2 uptakes estimated from long-term measurements of atmospheric CO_2 mole fraction, $\delta^{13}C$, and $\delta(O_2/N_2)$ at Ny-Ålesund, Svalbard. Journal of Geophysic Research-Biogeology 122: 1192-1202.

Hey MH (1954). A new review of chlorites. Mineralogical Magazine 30: 44-58.

Hyppolito T, Angiboust S, Juliani C, Glodny J, Garcia-Casco A et al. (2016). Eclogite-amphibolite-and blueschist-facies rocks from Diego de Almagro Island (Patagonia): episodic accretion and thermal evolution of the Chilean subduction interface during the Cretaceous. Lithos 264: 422-440.

Lanari P, Engi M (2017). Local bulk composition effects on metamorphic mineral assemblages. Review Mineralogy and Geochemistry 83:55–102.

Lanari P, Vidal O, De Andrade V, Dubacq B, Lewin E et al. (2014c). XMapTools: A MATLAB©- based program for electron microprobe X-ray image processing and geothermobarometry. Computer Geoscience 62: 227-240.

Leake BA, Woolley AR, Arps CES, Birch WD, Gilbert MC et al. (1997). Nomenclature of amphiboles. Report of the Subcommittee on Amphiboles of the International Mineralogical Association Commission on New Minerals and Mineral Names. European Journal of Mineralogy 9: 623-651.

Lopez-Carmona A, Abati J, Reche J (2010). Petrologic modeling of chloritoid–glaucophane schists from the NW Iberian Massif. Gondwana Research 17: 377-391.

Martin LAJ, Hermann J, Gauthiez-Putallaz L, Whitney DL, Vitale-Brovarone A et al. (2014). Lawsonite geochemistry and stability: Implication for trace element and water cycles in subduction zones. Journal of Metamorphic Geology 32: 455-478.

Mulcahy SR, Vervoort JD, Renne PR (2014). Dating subduction-zone metamorphism with combined garnet and lawsonite Lu–Hf geochronology. Journal of Metamorphic Geology 32:515-533.

Morimoto N, Fabries J, Ferguson AK, Ginzburg IV, Ross M et al. (1988). Nomenclature of pyroxenes. American Mineralogist 73: 1123-1133.

Oberhänsli R, Candan O, Wilke F (2010). Geochronological Evidence of Pan-AfricanEclogites from the Central Menderes Massif, Turkey. Turkish Journal of Earth Science 19: 431-447.

Oberhänsli R, Monie P, Candan O, Warkus F, Partzsch JH et al. (1998). The age of blueschist metamorphism in the Mesozoic cover series of the Menderes Massif. Schweizerische Mineralogische und Petrographische Mitteilungen 78: 309-316.

Oberhänsli R, Partzsch JH, Candan O, Çetinkaplan M (2001). First occurrence of Fe-Mg-carpholite documenting a high-pressure metamorphism in metasediments of the Lycian Nappes, SW–Turkey. International Journal of Earth Science 89: 867-873.

Okay AI (1980). Mineralogy, petrology and phase relation of glaucophane–lawsonite zone blueschists from the Tavşanlı region, Northwest Turkey. Contributions to Mineralogy and Petrology 72: 243-255.

Okay AI (1982). Incipient blueschist metamorphism and metasomatism in the Tavşanlı region, Northwest Turkey. Contributions to Mineralogy and Petrology 79: 361-367.

Okay AI (1984a). Distribution and characteristics of the northwest Turkish blueschists. In: Dixon, J.E., Robertson, A.H.F. (editors.), The Geological Evolution of the Eastern Mediterranean vol. 17. London, UK: Geological Society of London, pp. 455-466.

Okay AI (1984b). Kuzeybatı Anadolu'da yer alan metamorfik kuşaklar, in Proceedings, Ketin Symposium; Ankara, Turkey. pp. 83-92. (in Turkish).

Okay AI (1986). High-pressure/low-temperature metamorphic rocks of Turkey. Geological Society of America 164: 333-347.

Okay AI (2002). Jadeite-Chloritoid-glaucophane-lawsonite blueschists in North-west Turkey: unusually high P/T ratios in continental crust. Journal of Metamorphic Geology 20: 757-768.

Okay AI, Kelley SP (1994). Tectonic setting, petrology and geochronology of jadeite+glaucophane and chloritoid+glaucophane schists from northwest Turkey. Journal of Metamorphic Geology 12:455-466.

Okay AI, Harris NBW, Kelley SP (1998). Blueschist exhumation along a Tethyan suture in northwest Turkey. Tectonophysics 285: 275-299.

Plunder A, Agard P, Chopin C, Okay AI (2013). Geodynamics of the Tavşanlı zone, western Turkey: Insights into subduction/obduction processes. Tectonophysics 608: 884-903.

Pognante U (1989). Tectonic implications of lawsonite formation in the Sesia zone (Western Alps). Tectonophysics 162: 219-227.

Poli S, Franzolin E, Fumagalli P, Crottini A (2009). The transport of carbon and hydrogen in subducted oceanic crust: An experimental study to 5 GPa. Earth and Planetary Science Letters 278: 350-360.

Poli S, Schmidt MW (2004). Experimental subsolidus studies on epidote minerals. Review Mineralogy and Geochemistry 56: 171-195.

Pourteau A, Scherer EE, Schorn S, Bast R, Schmidt A et al. (2019). Thermal evolution of an ancient subduction interface revealed by Lu-Hf garnet geochronology, Halilbağı Complex (Anatolia). Geoscience Frontiers 10 (1): 127-148.

Rimmele G, Para T, Goffe B, Oberhänsli R, Jolivet L et al. (2005). Exhumation paths of high-pressure–low-temperature metamorphic rocks from the Lycian Nappes and the Menderes Massif (SW Turkey): a multiequilibrium approach. Journal of Petrology 46 (3): 641-669.

Ruh JB, Le Pourhiet L, Agard P, Burov E, Gerya T (2015). Tectonic slicing of subducting oceanic crust along plate interfaces: Numerical modeling. Geochemistry, Geophysics, Geosystems 16 (10): 3505-3531

Scheffler F, Oberhänsli R, Pourteau A, Di Luca M, Candan O (2015). The Rosetta Marbles from Fesleğen, Ören Unit, SW Anatolia. International Journal of Earth Science 103: 485-486.

Schmidt MW, Poli S (1994). The stability of lawsonite and zoisite at high pressures: Experiments in CASH to 92 kbar and implications for the presence of hydrous phases in subducted lithosphere. Earth and Planetary Science Letters 124 (1-4): 105-118.

Seaton NC, Whitney D, Teyssier C, Toraman E, Heizler MT (2009). Recrystallization of high pressure marble (Sivrihisar, Turkey). Tectonophysics 479: 241-253.

Topuz G, Okay AI (2014). Prograde calcite to aragonite transformation in the Gümüşyeniköy micriticlime stones (Tavşanlı, NW Turkey). International Journal of Earth Sciences 103(8): 2271-2272.

Topuz G, Okay AI, Altherr R, Satır M, Schwarz H (2008). Late Cretaceous blueschist facies metamorphism in southern Thrace (Turkey) and its geodynamic implications. Journal of Metamorphic Geology 26: 895-913.

Tsujimori T, Ernst WG (2014). Lawsonite blueschists and lawsonite eclogites as proxies for paleo-subduction zone processes: a review. Journal of Metamorphic Geology 32: 437-454.

Vitale Brovarone A, Alard O, Beyssac O, Martin L, Picatto M (2014). Lawsonite metasomatism and trace element recycling in subduction zones. Journal of Metamorphic Geology 32: 489-514.

Vitale Brovarone A, Beyssac O, Malavieille J, Molli G, Beltrando M, Compagnoni R (2013). Stacking and metamorphism of continuous segments of subducted lithosphere in a high-pressure wedge: the example of Alpine Corsica (France). Earth Science Reviews 116: 35-56.

Warren CJ, Waters DJ (2006). Oxidized eclogites and garnet-blueschists from Oman: P–T path modelling in the NCFMASHO system. Journal of Metamorphic Geology 24: 783-802.

Wei CJ, Clarke GL (2011). Calculated phase equilibria for MORB compositions: a reappraisal of the metamorphic evolution of lawsonite eclogite. Journal of Metamorphic Geology 29: 939-952.

Whitney D, Davis PB (2006). Why is lawsonite eclogite so rare? Metamorphism and preservation of lawsonite eclogite, Sivrihisar, Turkey. Geology 34(6): 473-476.

Whitney D, Evans BW (2010). Abbreviations for names of rock-forming minerals. American Mineralogist 95(1): 185-187.

Zack T, Rivers T, Brumm R, Kronz A (2004). Cold subduction of oceanic crust: implications from a lawsonite eclogite from the Dominican Republic. European Journal of Mineralogy 16: 909-916.